SLAC-PUB-16863

Joint Measurement of Lensing-Galaxy Correlations Using SPT and DES SV Data

E. Baxter[1⋆], J. Clampitt[1], T. Giannantonio[2,3,4], S. Dodelson[5,6], B. Jain[1], D. Huterer[7], L. Bleem[6,8,9], T. Crawford[6,10], G. Efstathiou[2,3], P. Fosalba[11], D. Kirk[12], J. Kwan[1], C. Sánchez[13], K. Story[14,15], M. A. Troxel[16], T. M. C. Abbott[17], F. B. Abdalla[12,18], R. Armstrong[19], A. Benoit-Lévy[12,20,21], B. Benson[5,6,10], G. M. Bernstein[1], R. A. Bernstein[22], E. Bertin[20,21], D. Brooks[12], J. Carlstrom[6,8,10], A. Carnero Rosell[23,24], M. Carrasco Kind[25,26], J. Carretero[11,13], R. Chown[27], M. Crocce[11], C. E. Cunha[15], L. N. da Costa[23,24], S. Desai[28,29], H. T. Diehl[5], J. P. Dietrich[28,29], P. Doel[12], A. E. Evrard[7,30], A. Fausti Neto[23], B. Flaugher[5], J. Frieman[5,6], D. Gruen[15,31], R. A. Gruendl[25,26], G. Gutierrez[5], T. de Haan[27,32], G. Holder[27], K. Honscheid[33,34], Z. Hou[6,8], D. J. James[17], K. Kuehn[35], N. Kuropatkin[5], M. Lima[23,36], M. March[1], J. L. Marshall[37], P. Martini[33,38], P. Melchior[19], C. J. Miller[7,30], R. Miquel[13,39], J. J. Mohr[28,29,40], B. Nord[5], Y. Omori[27], A. A. Plazas[41], C. Reichardt[42], A. K. Romer[43], E. S. Rykoff[15,31], E. Sanchez[44], I. Sevilla-Noarbe[25,44], E. Sheldon[45], R. C. Smith[17], M. Soares-Santos[5], F. Sobreira[5,23], E. Suchyta[1], A. Stark[46], M. E. C. Swanson[26], G. Tarle[7], D. Thomas[47], A. R. Walker[17], R. H. Wechsler[14,15,31]

Author affiliations are listed at the end of this paper

Last updated 1 July 2016

ABSTRACT

We measure the correlation of galaxy lensing and cosmic microwave background lensing with a set of galaxies expected to trace the matter density field. The measurements are performed using pre-survey Dark Energy Survey (DES) Science Verification optical imaging data and millimeter-wave data from the 2500 square degree South Pole Telescope Sunyaev-Zel'dovich (SPT-SZ) survey. The two lensing-galaxy correlations are jointly fit to extract constraints on cosmological parameters, constraints on the redshift distribution of the lens galaxies, and constraints on the absolute shear calibration of DES galaxy lensing measurements. We show that an attractive feature of these fits is that they are fairly insensitive to the clustering bias of the galaxies used as matter tracers. The measurement presented in this work confirms that DES and SPT data are consistent with each other and with the currently favored ΛCDM cosmological model. It also demonstrates that joint lensing-galaxy correlation measurement considered here contains a wealth of information that can be extracted using current and future surveys.

Key words: Cosmic background radiation – gravitational lensing: weak – large-scale structure of the Universe

1 INTRODUCTION

Gravitational lensing of light from cosmological sources is sensitive to both the matter content of the Universe

⋆ E-Mail: ebax@sas.upenn.edu

This material is based upon work supported by the U.S. Department of Energy, Office of Science, under Contract No. DE-AC02-76SF00515.

and to its geometry (for a review see Bartelmann 2010). A common approach to measuring gravitational lensing with the goal of constraining cosmology is to correlate some measure of the lensing strength with a tracer of the matter density field, such as galaxies. One advantage of lensing-tracer cross-correlation measurements is that they typically have much higher signal-to-noise than lensing-lensing correlations. Gravitational lensing of the cosmic microwave background (CMB), for instance, was first detected (Smith et al. 2007) by cross-correlating noisy CMB lensing maps with a catalog of radio galaxies. Similarly, in the context of galaxy lensing, the cross-correlation of lensing induced shearing of background galaxies with the positions of foreground galaxies (known as galaxy-galaxy lensing) was detected (Brainerd et al. 1996) before shear-shear correlations (Bacon et al. 2000; Kaiser et al. 2000; Van Waerbeke et al. 2000; Wittman et al. 2000). Furthermore, lensing-tracer cross-correlation measurements are typically less sensitive to additive systematic errors since these will tend to average to zero in the cross-correlation (assuming the sources of systematic error are uncorrelated between the lensing measurements and the tracer measurements, often a reasonable approximation). Henceforth, we will refer to sources of light used to measure gravitational lensing distortion as *sources*, and we will refer to objects used as tracers of the matter density field as *tracers*.

In this work, we perform a joint measurement of two lensing-tracer cross-correlations that involve different sources, but the same set of tracer galaxies. The first source that we consider is the CMB, which originates from a redshift of $z \sim 1100$. Gravitational lensing of the CMB is typically measured in terms of the convergence, κ, which quantifies the amount of lensing-induced dilation of an image (defined rigorously in §2). We measure the angular correlation, $w^{\kappa g}(\theta)$, between the CMB-derived κ and the tracer galaxies. The second source that we consider is a set of galaxies at redshifts $0.8 \lesssim z \lesssim 1.3$. Gravitational lensing of galaxies is typically measured in terms of the shear, γ, which quantifies the amount of lensing-induced stretching of an image (defined rigorously in §2). We measure the angular correlation, $w^{\gamma_T g}(\theta)$, between the tracer galaxies and the tangential shear, γ_T, which describes the component of the shear perpendicular to the line connecting the image of a source galaxy and a tracer galaxy. The superscript g in both $w^{\kappa g}(\theta)$ and $w^{\gamma_T g}(\theta)$ is intended to remind the reader that these correlations are with respect to the *same* set of tracer galaxies.

Because gravitational lensing is sensitive to the matter content of the Universe and to its geometry, both $w^{\kappa g}(\theta)$ and $w^{\gamma_T g}(\theta)$ are sensitive to cosmological parameters. However, both cross-correlations also depend on the *bias*, $b(k, z)$, of the tracer galaxies, defined as the square root of the ratio of the tracer power spectrum to the underlying matter power spectrum:

$$b(k, z) \equiv \sqrt{P_{gg}(k, z)/P_{mm}(k, z)}, \tag{1}$$

where P_{gg} is the tracer galaxy power spectrum and P_{mm} is the matter power spectrum, both evaluated at wavenumber k and redshift z. At large scales, the bias becomes scale-independent and is therefore completely degenerate with the amplitude of the matter power spectrum, A_s. Other cosmological parameters, such as Ω_M (the matter density parameter) are also degenerate with the large scale bias. At small scales, the bias may become scale-dependent and can therefore be degenerate with additional cosmological parameters. For a single lensing-tracer cross-correlation measurement, degeneracies between the tracer bias and the cosmological parameters result in a degradation of cosmological constraints.

A joint measurement of two lensing-tracer cross-correlations that uses different sources but the same set of tracer objects can break the degeneracy between bias and cosmological parameters. This basic idea has been suggested by several authors. Jain & Taylor (2003), for instance, propose measuring $w^{\gamma_T g}(\theta)$ with source galaxies in multiple redshift bins at high redshift around a single set of tracer galaxies at low redshift. They show that in the limit that the tracer galaxies are narrowly distributed in redshift, the ratio of the shear-tracer correlation for one source bin to that of a different source bin is completely insensitive to the bias of the tracer galaxies. Similarly, Das & Spergel (2009) propose measuring the ratio of two lensing-tracer cross-power spectra, $C_\ell^{\kappa_{\rm Gal} g}/C_\ell^{\kappa_{\rm CMB} g}$, where $C_\ell^{\kappa_{\rm Gal} g}$ is the cross-power spectrum between a galaxy-lensing derived κ map and a set of tracer galaxies, g, and $C_\ell^{\kappa_{\rm CMB} g}$ is the same quantity for a CMB-lensing derived κ map. Again in the limit that the tracer galaxies are narrowly distributed in redshift, the galaxy bias will cancel in this ratio, making it a powerful cosmological probe. An attractive feature of combining CMB and galaxy lensing measurements (compared to the galaxy-lensing-only measurement proposed by Jain & Taylor 2003) is that the large distance to the CMB last scattering surface makes the lensing ratio more sensitive to cosmological parameters (Hu et al. 2007).

Note that unlike Das & Spergel (2009), we consider here a *joint fit* to $w^{\kappa g}(\theta)$ and $w^{\gamma_T g}(\theta)$ rather than the ratio of two lensing-tracer cross-correlations. Performing a joint fit has several significant advantages over the ratio measurement. For one, the joint fit can be applied directly to $w^{\kappa g}(\theta)$ and $w^{\gamma_T g}(\theta)$. This is advantageous because CMB lensing is typically measured in terms of κ, while galaxy lensing is typically measured in terms of γ_T, and the conversion from γ_T to κ (or vice versa) is difficult and potentially susceptible to systematic biases. Furthermore, while the probability distribution functions of the $w^{\kappa g}(\theta)$ and $w^{\gamma_T g}(\theta)$ measurements can be reasonably approximated as multivariate Gaussians, the ratio of two noisy Gaussian quantities is no longer Gaussian distributed and is therefore difficult to model. Additionally, when the tracer galaxies do not have a very narrow redshift distribution, the exact cancellation of the tracer bias in the ratio does not hold, and the interpretation of the ratio measurement becomes difficult. Finally, the joint fit contains more information than the ratio since the ratio is computed from a combination of the two individual $w^{\kappa g}(\theta)$ and $w^{\gamma_T g}(\theta)$ measurements.

In addition to being a powerful probe of cosmology, the joint measurement of $w^{\kappa g}(\theta)$ and $w^{\gamma_T g}(\theta)$ can also be used to constrain sources of systematic error that may impact either of the two measured lensing-tracer correlations. Sources of systematic error that affect the CMB-derived κ map are unlikely to have the same effect on the galaxy-lensing derived γ_T and vice versa. Consequently, joint measurement of both $w^{\kappa g}(\theta)$ and $w^{\gamma_T g}(\theta)$ can be used to constrain systematic errors in the lensing measurements that would be

difficult (or impossible) to measure with a single lensing-tracer cross-correlation (Das et al. 2013; Vallinotto 2013). Recently, Liu et al. (2016) used the joint measurement of galaxy and CMB lensing around a set of tracer galaxies to constrain the multiplicative bias of lensing shear measurements made by the Canada-France-Hawaii Telescope Lensing Survey. In addition to systematic errors in the lensing measurements, the joint observable here is also sensitive to systematic errors in the redshift distributions of the source and tracer galaxies. For DES (and other ongoing and future optical surveys), the redshifts of the vast majority of galaxies are determined photometrically. Because photometric redshift estimation is challenging, potentially subject to systematic errors, and requires large spectroscopic training sets (e.g. Hildebrandt et al. 2010), the possibility of using the joint measurement of $w^{\kappa g}(\theta)$ and $w^{\gamma_T g}(\theta)$ to constrain galaxy redshift distributions is appealing.

In this work, we measure $w^{\kappa g}(\theta)$ and $w^{\gamma_T g}(\theta)$ using data from the South Pole Telescope (SPT) and pre-survey Dark Energy Survey (DES) Science Verification (SV) imaging. We perform a joint fit to the measured $w^{\kappa g}(\theta)$ and $w^{\gamma_T g}(\theta)$ to extract constraints on cosmological parameters, the photometric redshift distribution of the tracer galaxies, and systematic biases in our measurements of tangential shear (henceforth, we will refer to systematic biases as *systematics* to eliminate confusion with the clustering bias). Ultimately, DES will observe roughly 5000 sq. deg. of the Southern sky; the SV data used in this work, however, is restricted to a small fraction (roughly 3%) of the full survey area. Because of the small area of the DES SV survey we do not expect to obtain highly competitive constraints in this preliminary analysis. For this reason, we treat the measurement presented here mainly as a consistency check between SPT and DES data and as a proof-of-principle for the joint $w^{\kappa g}(\theta)$ and $w^{\gamma_T g}(\theta)$ measurement.

Our analysis builds upon other recently published analyses of DES SV data. The galaxy catalog used here was constructed and tested for systematic effects in Crocce et al. (2016) and references therein. The galaxy shear catalog used in this work was extensively tested in Jarvis et al. (2015), while galaxy-galaxy lensing measurements and systematics tests were performed in Clampitt et al. (2016). Additionally, the cross-correlation between the galaxy catalog used in this work and the SPT-derived CMB κ map was first measured in Giannantonio et al. (2016). These and other DES SV papers provided key methodological ingredients that support the analysis presented here.

In principle, one could imagine expanding the scope of the joint $w^{\kappa g}(\theta)$ and $w^{\gamma_T g}(\theta)$ measurement considered here to include additional correlations between galaxies, galaxy shear and CMB κ. In fact, all of the other possible correlations involving these observables have already been measured by DES and SPT: the shear-shear correlation was measured in The Dark Energy Survey Collaboration et al. (2015), the galaxy-galaxy correlation was measured in Crocce et al. (2016), and the correlation between CMB κ and galaxy shear was measured in Kirk et al. (2015). We have two reasons for restricting the analysis in this work to $w^{\kappa g}(\theta)$ and $w^{\gamma_T g}(\theta)$. First, because $w^{\kappa g}(\theta)$ and $w^{\gamma_T g}(\theta)$ are cross-correlations between different observable types—namely galaxy positions and gravitational lensing distortions—they are immune to several observational systematics. Second, one of the main goals of this work is to show how degeneracies between galaxy bias and parameters of interest are broken by performing a joint measurement of galaxy and CMB lensing. Since neither the shear-shear correlation nor the correlation between galaxy shear and CMB κ depend on galaxy bias, their inclusion in this analysis is not essential. Since we are not attempting to generate competitive cosmological constraints in this work, leaving out these additional correlations is not a serious handicap for our analysis.

The outline of the paper is as follows. In §2 we introduce the necessary gravitational lensing formalism; in §3 we describe the datasets used in this work; in §4 we describe the process of measuring $w^{\kappa g}(\theta)$ and $w^{\gamma_T g}(\theta)$; in §5 we describe our models for the data and the process of extracting constraints on the parameters of these models. Our results are presented in §6 and conclusions are given in §7.

2 FORMALISM

We are interested in the cross-correlations of CMB lensing and galaxy lensing with a single set of tracer galaxies. We quantify CMB lensing using the lensing convergence, κ, as there is a well developed literature on estimating κ from CMB temperature maps. We quantify galaxy lensing with the lensing shear, γ, as this quantity can be measured directly from the distortion of galaxy shapes. In principle, one could convert κ to γ or vice versa, but we do not take this approach here.

The convergence κ is given by a weighted integral of the distribution of matter along the line of sight. Following the notation of Jain & Taylor (2003), κ in the direction specified by the unit vector $\hat{n}$ is

$$\kappa(\hat{n}) = \frac{3}{2c^2}\Omega_M H_0^2 \int d\chi\, g(\chi) \frac{\delta(\chi\hat{n},\chi)}{a(\chi)}, \tag{2}$$

where χ is the comoving distance, $a(\chi)$ is the scale factor, $\delta(\chi\hat{n},\chi)$ is the overdensity evaluated along the line of sight, and we have assumed a spatially flat Universe. Here $g(\chi)$ is the lensing weight function:

$$g(\chi) = \chi \int_\chi^\infty d\chi' \frac{(\chi'-\chi)}{\chi'} W^s(\chi'), \tag{3}$$

where $W^s(\chi)$ is the normalized distribution of the sources in comoving distance. The weight $W^s(\chi)$ is given in terms of the distribution of sources as a function of redshift, $N^s(z)$, by

$$W^s(\chi) = \frac{1}{\int dz' N^s(z')} \frac{dz}{d\chi} N^s(z). \tag{4}$$

We define $n^g(\hat{n})$ as the projected density of tracer galaxies in direction $\hat{n}$ and $\delta n^g(\hat{n}) = (n^g(\hat{n}) - \bar{n}^g)/\bar{n}^g$. The angular correlation between κ and the tracer galaxies is then $w^{\kappa g}(\theta) = \langle \delta n^g(\hat{n}) \kappa(\hat{n}') \rangle$, where the average is taken over all pairs of points chosen so that the angular separation between $\hat{n}$ and $\hat{n}'$ is θ. As we will discuss below, filtering of the CMB-derived κ field in harmonic space means that it is useful to express $w^{\kappa g}(\theta)$ in terms of the cross-power spectrum, $C_\ell^{\kappa g}$, between the CMB-derived κ and the tracer galaxies:

$$w^{\kappa g}(\theta) = \sum_{l=0}^{\infty} \left(\frac{2l+1}{4\pi}\right) P_l(\cos\theta) C_\ell^{\kappa g}, \tag{5}$$

where P_l is the Legendre polynomial of order l. This expression is exactly correct on the curved sky. At small angular scales, the Limber approximation (Limber 1953; Kaiser 1992) is valid and we can relate $C_\ell^{\kappa g}$ to the matter power spectrum, $P(k,\chi)$, through

$$C_\ell^{\kappa g} = \frac{3\Omega_M H_0^2}{2c^2}\int d\chi \frac{1}{\chi^2}\frac{g^{\rm CMB}(\chi)}{a(\chi)} W^g(\chi) b\left(\frac{l}{\chi},\chi\right) P\left(\frac{l}{\chi},\chi\right), \quad (6)$$

where H_0 is the Hubble constant, $W^g(\chi)$ is the distribution of tracer galaxies in comoving distance (defined analogously to $W^s(\chi)$ for the sources), $b(k,\chi)$ is the clustering bias of the tracer galaxies (Bartelmann 2010; Das & Spergel 2009), and $g^{\rm CMB}(\chi)$ is the lensing weight function for the CMB source. Here, we make the approximation that all of the CMB light is sourced from a single comoving distance, χ_*, so that $W_s(\chi) = \delta(\chi - \chi^*)$ and therefore $g^{\rm CMB}(\chi) = [\chi(\chi^* - \chi)/\chi^*]\,\Theta(\chi^* - \chi)$, where $\Theta(\chi)$ is the Heaviside step function. Our convention is that the forward Fourier transform is defined by

$$f(\vec{x}) = \int \frac{d^3k}{(2\pi)^3} e^{i\vec{k}\cdot\vec{x}} \tilde{f}(\vec{k}), \quad (7)$$

and the power spectrum is related to δ by

$$\langle \delta(\vec{k})\delta(\vec{k}')\rangle = (2\pi)^3\delta^3(\vec{k}-\vec{k}')P(k). \quad (8)$$

The angular correlation between the shears of the source galaxies and the tracer galaxies is measured in terms of the tangential shear, γ_T, the component of the shear orthogonal to the line connecting the source galaxy at which the shear is measured to the tracer galaxy:

$$\gamma_T = -\gamma_1\cos(2\varphi) - \gamma_2\sin(2\varphi), \quad (9)$$

where γ_1 and γ_2 are the components of the shear, γ, in a Cartesian basis, and φ is the position angle of the tracer galaxy relative to the source galaxy in the same Cartesian basis. Analogously to $w^{\kappa g}(\theta)$, $w^{\gamma_T g}(\theta) = \langle \delta n^g(\hat{n})\gamma_T(\hat{n}')\rangle$, where again the average is taken over all pairs of points such that $\hat{n}$ and $\hat{n}'$ have an angular separation of θ. In this case, since we do not apply any filtering to the measured shear field, we can directly compute $w^{\gamma_T g}(\theta)$ using (Jain & Taylor 2003)

$$w^{\gamma_T g}(\theta) = \frac{3\Omega_M H_0^2}{4\pi c^2}\int d\chi \frac{g^s(\chi)}{a(\chi)} W^g(\chi)\int dk\, kb\,(\chi,k)\,P\,(\chi,k)\,J_2(k\chi\theta), \quad (10)$$

where $g^s(\chi)$ is the lensing weight for the source galaxies computed using Eq. 3 and Eq. 4. The W^g, $g^{\rm CMB}$ and g^s factors that enter into the computation of $w^{\kappa g}(\theta)$ and $w^{\gamma_T g}(\theta)$ are shown in Fig. 3. Note that W^g has different units than $g^{\rm CMB}$ and g^s; Fig. 3 is only intended to show the redshift ranges that contribute to these functions. For this reason, we have normalized all curves in Fig. 3 to the same maximum value.

Although this work is primarily concerned with the joint measurement of $w^{\kappa g}(\theta)$ and $w^{\gamma_T g}(\theta)$, it is instructive to consider the information content of the ratio of these two observables. For this purpose, we can re-write $w^{\kappa g}(\theta)$ in a form more similar to Eq. 10 (assuming no filtering is applied to the CMB-derived κ map). We have (Guzik & Seljak 2001)

$$w^{\kappa g}(\theta) = \frac{3\Omega_M H_0^2}{4\pi c^2}\int d\chi \frac{g^{\rm CMB}(\chi)}{a(\chi)} W^g(\chi)\int dk\, kb\,(\chi,k)\,P\,(k,\chi)\,J_0(k\chi\theta). \quad (11)$$

Note that the only differences between Eq. 11 and Eq. 10 are that the Bessel function of order two has been replaced by a Bessel function of order zero, and g^s has been replaced by $g^{\rm CMB}$. In the limit that the distribution of tracer galaxies in comoving distance is very narrow, it can be approximated with a Dirac δ-function: $W(\chi) = \delta(\chi - \chi^g)$. The ratio of the two observables then reduces to

$$\frac{w^{\kappa g}(\theta)}{w^{\gamma_T g}(\theta)} \approx \frac{g^{\rm CMB}(\chi^g)}{g^s(\chi^g)}\frac{\int dk\, kb(k,\chi^g)P(k,\chi^g)J_0(k\chi^g\theta)}{\int dk\, kb(k,\chi^g)P(k,\chi^g)J_2(k\chi^g\theta)}. \quad (12)$$

In the limit that the bias is scale-independent (valid at large scales), we have $b(k,\chi^g) = b(\chi^g)$ and the bias factors in the numerator and denominator of Eq. 12 will cancel. This cancellation makes the ratio $w^{\kappa g}(\theta)/w^{\gamma_T g}(\theta)$ independent of the scale-independent bias. This property is shared by the lensing ratios of Jain & Taylor (2003) and Das & Spergel (2009) (although in those cases, even the scale-dependent bias cancels in the lensing ratio).

While the scale-independent bias cancels in the ratio of our two observables, the factor $g^{\rm CMB}(\chi^g)/g^s(\chi^g)$ does not. This quantity contains information about the distances to the tracer galaxies, the source galaxies and the CMB; it therefore contains information about cosmological parameters that affect the geometry and expansion history of the Universe. Furthermore, information about systematics in either the CMB or galaxy-derived lensing measurements is not expected to cancel in the ratio since such systematics are likely uncorrelated between the CMB and galaxy lensing measurements. Finally, information about the redshifts of the source and tracer galaxies does not cancel in the ratio since this information is also contained in the $g^{\rm CMB}(\chi^g)/g^s(\chi^g)$ factor. Since the information content of $w^{\kappa g}(\theta)/w^{\gamma_T g}(\theta)$ is preserved in the joint $w^{\kappa g}(\theta)$ and $w^{\gamma_T g}(\theta)$ observable, we expect that our analysis of the joint observable will yield constraints on cosmology, systematics in the lensing measurements, and systematics in the galaxy redshift distributions, even if we allow for significant freedom in the tracer clustering bias.

3 DATA

The galaxy lensing measurements and the tracer galaxy catalog used in this work are both derived from DES SV imaging data which has been reduced from the raw survey data by the DES Data Management pipeline (Mohr et al. 2012; Desai et al. 2012). The CMB lensing data is derived from CMB temperature maps generated from SPT observations (Carlstrom et al. 2011). All of the data sets used in this work have been discussed in recently published literature. We therefore keep the discussion of the data somewhat brief, and direct the reader to the corresponding references for more detailed information.

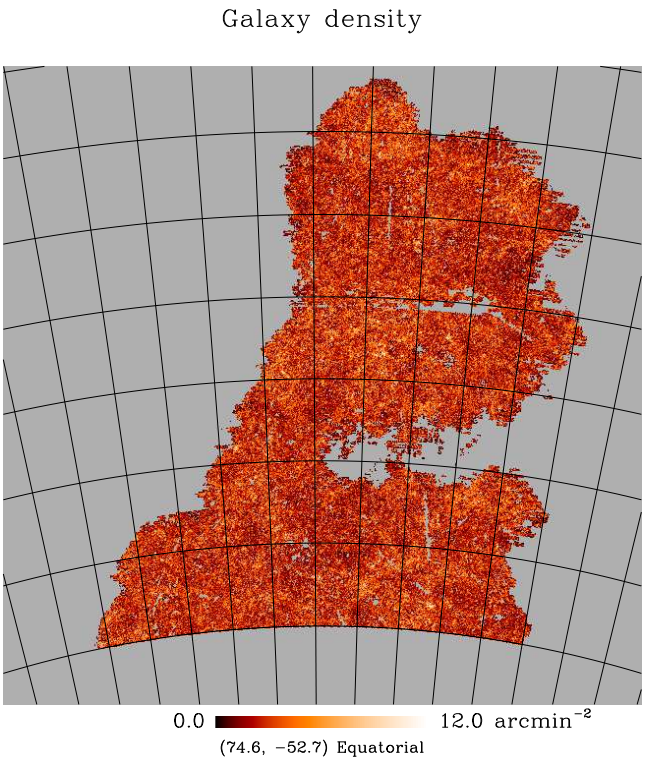

Figure 1. Density of tracer galaxies derived from the DES SV benchmark catalog plotted across the benchmark mask region. The density map is shown at Healpix $N_{\rm side} = 2048$ resolution (corresponding to a pixel size of $\sim 1.7'$). Note that although we plot the pixelized galaxy density here, $w^{\kappa g}(\theta)$ and $w^{\gamma_T g}(\theta)$ are computed using the un-pixelized tracer galaxy coordinates. Grey regions are either masked or outside the SV footprint. The grid lines are spaced 2.5 degrees apart in both R.A. and Dec. The coordinates $(74.6, -52.7)$ indicate the position of the map center in R.A. and Dec.

3.1 Data from the Dark Energy Survey

3.1.1 Tracer galaxy catalog

The catalog of galaxies used in this work as tracers of the matter density field is derived from DES SV optical imaging data. In total, DES SV imaging covers roughly 300 sq. deg. of the southern sky that was observed over 78 nights to near full-survey depth. The analysis here is restricted to the contiguous SPT-E field, which covers approximately 139 sq. deg. The DES SV final ('Gold') main galaxy catalog[1] contains 25,227,559 galaxies.

The tracer galaxy catalog that we use in this work is a subset of the full 'Gold' catalog that was selected by Crocce et al. (2016), and which is termed the *benchmark* selection. Briefly, the benchmark selection restricts the galaxy sample to $18 < i < 22.5$, where i is the `MAG_AUTO` quantity output by SExtractor (Bertin & Arnouts 1996). Several additional cuts are applied that, for instance, remove outliers in color space and remove stars that may be falsely classified as galaxies. The end result is a flux-limited sample of galaxies over an area of roughly 131 sq. deg. We use the corresponding benchmark galaxy angular mask in this analysis.

We use photometric redshift (photo-z) estimates for the purposes of selecting tracer and source galaxies, and also for computing the distributions of these two populations as a function of redshift (necessary when we model the measured lensing-tracer cross-correlations). The photo-z estimates used here are generated using the neural network-based `skynet2` code (Graff et al. 2014; Bonnett et al. 2015). `skynet2` computes the redshift probability distribution functions, $p(z)$, for each galaxy, given the photometric colors of that galaxy. Several photometric redshift estimation codes have been applied to DES SV galaxies. In this work we use the `skynet2` code as it performed the best in tests (Bonnett et al. 2015) and because this matches the choice made for the cosmic shear analysis of DES SV data by The Dark Energy Survey Collaboration et al. (2015). Bonnett et al. (2015) showed that `skynet2` was able to recover the mean redshift of samples of DES SV 'Gold' galaxies to typically better than 0.04. In general, though, DES SV science results have been shown to be quite robust to the choice of photo-z estimation code (e.g. Giannantonio et al. 2016; Crocce et al. 2016). Tracer and source galaxies are selected on the basis of the z value at which $p(z)$ peaks, z^p. For the tracers, we restrict the analysis to galaxies with $0.4 < z^p < 0.8$. The final tracer catalog contains approximately 1.3 million galaxies. A map of the tracer galaxy density across the benchmark mask is shown in Fig. 1.

The normalized $N(z)$ for the entire tracer catalog (i.e. the sum of all the individual $p(z)$) is shown in Fig. 2. The corresponding $W^g(\chi)$ is shown in Fig. 3, along with $g^s(\chi)$ and $g^{\rm CMB}(\chi)$ for comparison (note that we have transformed these quantities into functions of redshift for plotting purposes). It is clear from Fig. 3 that the tracer galaxy $W^g(\chi)$ peaks in a redshift range for which both $g^s(\chi)$ and $g^{\rm CMB}(\chi)$ have significant support. We note here that the measured $N(z)$ for the tracer catalog enters into the modeling of $w^{\kappa g}(\theta)$ and $w^{\gamma_T g}(\theta)$ through $W^g(\chi)$; as we will discuss more in §5.2.3, the dependence of $w^{\kappa g}(\theta)$ and $w^{\gamma_T g}(\theta)$ on $N(z)$ makes the joint measurement of these quantities a potentially powerful probe of galaxy redshift distributions.

3.1.2 Source galaxy shear catalog

The shear catalog used in this work to measure $w^{\gamma_T g}(\theta)$ is also derived from DES SV data[2]. Two shear catalogs were produced and tested extensively in Jarvis et al. (2015) (hereafter J15): the `ngmix`[3] (Sheldon 2014) and the `im3shape`[4] (Zuntz et al. 2013) catalogs. We use only the `ngmix` catalog in this work because they have a higher source number density. Shear estimation with `ngmix` was carried out using images in r, i, z bands. See J15 for more details and various tests of the shear pipeline. These choices are consistent with other analyses of DES SV data, including the

[1] `http://des.ncsa.illinois.edu/releases/sva1`

[2] The shear catalog is available at `http://des.ncsa.illinois.edu/releases/sva1`.

[3] `https://github.com/esheldon/ngmix`

[4] `https://bitbucket.org/joezuntz/im3shape`

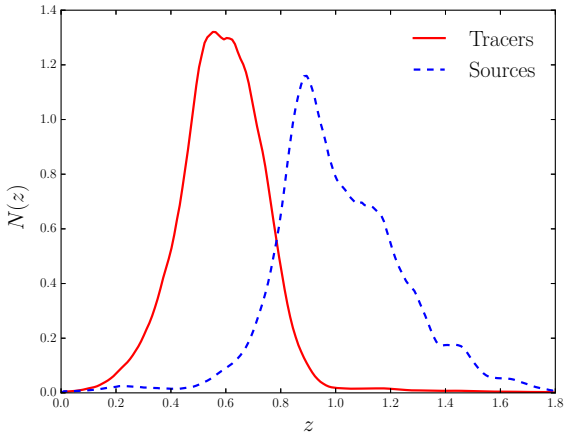

Figure 2. The normalized photometric redshift distributions, $N(z)$, for the tracer and source galaxy samples. The tracers are selected using a $0.4 < z^p < 0.8$ cut, where z^p is the redshift that maximizes the photometrically-determined redshift probability distribution for an individual galaxy, $p(z)$. The sources are selected using a $0.8 < z^p < 1.3$ cut.

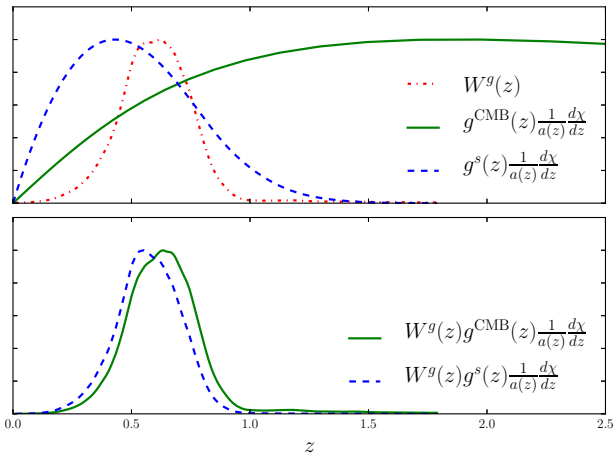

Figure 3. The W^g, $g^{\rm CMB}$ and g^s factors (and the relevant products of these factors) that enter into the computation of $w^{\kappa g}(\theta)$ (Eqs. 6 and 5) and $w^{\gamma_T g}(\theta)$ (Eq. 10). The figure is intended to illustrate the redshift ranges that contribute most to $w^{\kappa g}(\theta)$ and $w^{\gamma_T g}(\theta)$. All curves have been normalized to the same maximum value.

cosmology analysis of the cosmic shear two-point function (The Dark Energy Survey Collaboration et al. 2015). J15 performed many comparisons of the two shear pipelines, finding generally good agreement.

Particularly relevant for our purposes is the J15 comparison of the `im3shape` and `ngmix` tangential shear measurements. J15 measured tangential shears around luminous red galaxies using both pipelines over an angular range similar to that used here. J15 found that the ratio of the `im3shape` to `ngmix` tangential shear measurements is consistent with expectations from the application of these two shear pipelines to simulated data. The two pipelines can therefore be considered consistent with each other in their measurements of tangential shear. Note, though, that this ratio test does not preclude the possibility that both shear catalogs are biased by a similar multiplicative factor; we will consider how the joint measurement of $w^{\kappa g}(\theta)$ and $w^{\gamma_T g}(\theta)$ can be used to constrain such multiplicative biases in §5.2.2.

We restrict the source catalog to galaxies with $0.8 < z^p < 1.3$. This redshift cut and the various benchmark selections yield $\sim 947,000$ total source galaxies with a number density of $1.9/\mathrm{arcmin}^2$. The photometrically-determined $N(z)$ for the source galaxies is shown in Fig. 2.

3.2 Data from the South Pole Telescope

The CMB κ maps used in this work were derived from CMB temperature data taken as part of the 2500 square degree South Pole Telescope Sunyaev-Zel'dovich (SPT-SZ) survey (Story et al. 2013). Many observations at 150 GHz of the SPT-E region were combined using inverse-variance weighting to generate a $25^\circ \times 25^\circ$ CMB temperature map. A CMB κ map was then derived from the CMB temperature map following the methods outlined in van Engelen et al. (2012), which rely on the quadratic estimator of Hu (2001) and Hu & Okamoto (2002). The CMB κ map was pixelized using a Healpix (Górski et al. 2005) grid with $N_{\rm side} = 2048$. The processed SPT CMB lensing maps used here are identical to those used in Giannantonio et al. (2016) and we refer the reader to that work for more details. The same maps were also used in the cross-correlation of CMB lensing with galaxy lensing measurement of Kirk et al. (2015). As in Giannantonio et al. (2016), we filter the pixelized CMB κ map to remove modes with $\ell < 30$ and also apply Gaussian-beam smoothing with $\theta_{\rm FWHM} = 5.4'$. In our analysis, we use the CMB κ map across the full SPT-E region without applying any additional masking. This means that the tracer galaxies are correlated with regions of the CMB κ map that lie outside of the benchmark mask discussed §3.1.1. The CMB κ map is plotted in Fig. 4. To aid with visualization and comparison to Fig. 1 we have applied additional smoothing to the κ map in Fig. 4 and have restricted the plot to the benchmark mask.

Planck Collaboration et al. (2015a) have also released a CMB-lensing-derived κ map that could be used to measure $w^{\kappa g}(\theta)$. As demonstrated in Giannantonio et al. (2016), the signal-to-noise of $w^{\kappa g}(\theta)$ measured using the benchmark galaxies and the Planck κ map is only slightly lower than the signal-to-noise of the same measurement using the SPT κ map. However, because this work is intended as a "proof of concept" for the joint $w^{\kappa g}(\theta)$ and $w^{\gamma_T g}(\theta)$ measurement, we postpone a joint measurement of $w^{\kappa g}(\theta)$ and $w^{\gamma_T g}(\theta)$ with Planck and DES data to future work based on a larger DES sample.

4 $W^{\kappa G}(\theta)$ AND $W^{\gamma_T G}(\theta)$ MEASUREMENTS

We measure $w^{\kappa g}(\theta)$ using the CMB κ map described in §3.2 and the galaxy tracer catalog described in §3.1.1. We estimate $w^{\kappa g}(\theta)$ with

$$\hat{w}^{\kappa g}(\theta_\alpha) \quad = \quad \bar{\kappa}_\alpha - \bar{\kappa}_\alpha^{\rm rand}, \qquad (13)$$

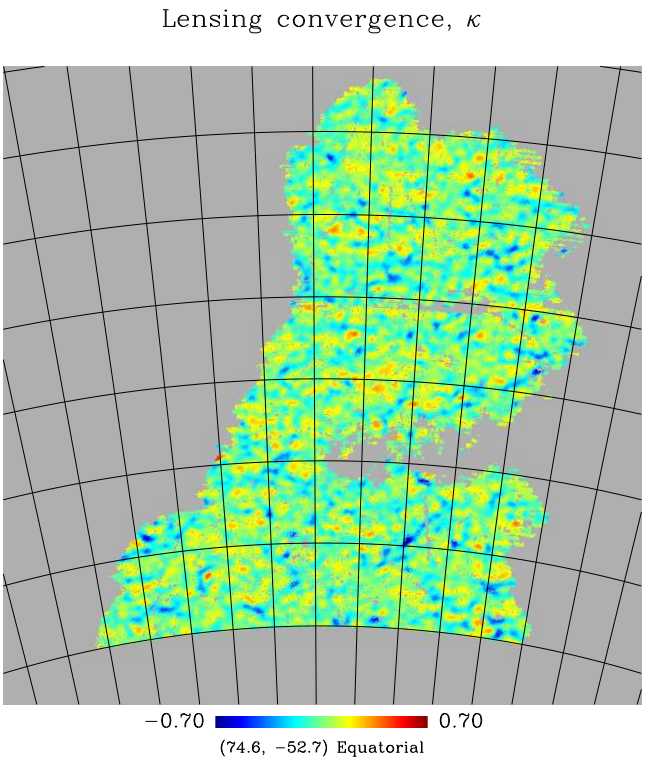

Figure 4. The filtered lensing convergence, κ, derived from SPT CMB data across the benchmark mask region. As described in the text, the κ map is high-pass filtered to $\ell > 30$ and is smoothed with a Gaussian beam with $\theta_{\rm FWHM} = 5.4'$. For this plot we have also applied a Gaussian beam with $\theta_{\rm FWHM} = 10'$ to improve the visualization. The map is shown at Healpix $N_{\rm side} = 2048$ resolution. Note that although we have applied the benchmark mask in making this plot, the full SPT-derived κ map is used when measuring $w^{\kappa g}(\theta)$. Coordinate system and gridlines are the same as those in Fig. 1.

where θ_α is the (logarithmic) center of the α angular bin and

$$\bar{\kappa}_\alpha = \frac{\sum_i^{N_{\rm pix}} \sum_j^{N_{\rm tracer}} \kappa_j f_{ij\alpha}}{\sum_i^{N_{\rm pix}} \sum_j^{N_{\rm tracer}} f_{ij\alpha}}. \quad (14)$$

Here, $N_{\rm pix}$ is the number of pixels in the κ map, $N_{\rm tracer}$ is the number of tracer galaxies, and κ_j is the value of κ in the jth pixel. The weight function $f_{ij\alpha} = 1$ if the angular separation between tracer galaxy i and pixel j is in angular bin α and $f_{ij\alpha} = 0$ otherwise. The quantity $\bar{\kappa}_\alpha^{\rm rand}$ in Eq. 13 is defined similarly to $\bar{\kappa}_\alpha$, except that the tracer catalog is replaced by a catalog of randomly distributed points that have the same angular mask as the tracer galaxies. By subtracting $\bar{\kappa}_\alpha^{\rm rand}$ from $\bar{\kappa}_\alpha$ we correct for any mask and pixelization effects. The sums in Eq. 14 are computed using the publicly available tree code `TreeCorr`[5] (Jarvis et al. 2004).

We measure $w^{\gamma_T g}(\theta)$ using the shear catalog described in §3.1.2 and the tracer galaxy catalog described in §3.1.1. The estimator for $w^{\gamma_T g}(\theta)$ is similar to that for $w^{\kappa g}(\theta)$:

$$\hat{w}^{\gamma_T g}(\theta_\alpha) \quad = \quad \bar{\gamma}_\alpha - \bar{\gamma}_\alpha^{\rm random}, \quad (15)$$

[5] `https://github.com/rmjarvis/TreeCorr`

where the γ are understood to be tangential shears (dropping the subscript T temporarily for notational convenience), and

$$\bar{\gamma}_\alpha = \frac{\sum_i^{N_{\rm source}} \sum_j^{N_{\rm tracer}} \gamma_{ij} f'_{ij\alpha}}{\sum_i^{N_{\rm source}} \sum_j^{N_{\rm tracer}} f'_{ij\alpha}}. \quad (16)$$

The sum over i now runs over all source galaxies (instead of pixels) and γ_{ij} is the tangential shear of source galaxy i measured with respect to tracer galaxy j. The weight function $f'_{ij\alpha}$ is defined such that $f'_{ij\alpha} = 1/(\sigma^2_{\rm shape} + \sigma^2_{{\rm m},i})$ when the angular separation between source galaxy i and tracer galaxy j is in angular bin α and $f'_{ij\alpha} = 0$ otherwise. Here, $\sigma_{{\rm m},i}$ is the shape measurement error of the ith source galaxy, and $\sigma_{\rm shape} = 0.22$ is the intrinsic shape noise of the source galaxies. Again we use `TreeCorr` to calculate these sums.

γ_T is expected to be robust to spatially constant additive shear systematics since these will cancel when averaging over sources that are isotropically distributed around tracer galaxies. This is one of the main motivations for measuring $w^{\gamma_T g}(\theta)$ rather than converting γ_T to κ and performing a κ-tracer cross-correlation (the γ to κ conversion process is not robust to additive systematics). Furthermore, by subtracting γ_T measured around random points as in Eq. 15, we remove the contribution to the tangential shear measurement from spatially varying additive systematics and edge effects.

We perform both the $w^{\kappa g}(\theta)$ and $w^{\gamma_T g}(\theta)$ measurements in $N_\theta = 10$ angular bins logarithmically distributed between $\theta_{\rm min} = 3'$ and $\theta_{\rm max} = 50'$. Our choice of $\theta_{\rm max}$ is set by the size of our jackknife regions (see below), while the choice of $\theta_{\rm min}$ is motivated in §5.1.1.

We measure the covariance matrix, C_{ij}, of our joint observable using a jackknife sampling approach; the indices i and j here run from one to $2N_\theta$, the length of our joint data vector. First, the survey region is divided into $N_{\rm JK} = 200$ roughly equal-area regions. The $w^{\kappa g}(\theta)$ and $w^{\gamma_T g}(\theta)$ measurements are then repeated with each of the jackknife regions removed. The full covariance matrix for the joint $w^{\kappa g}(\theta)$ and $w^{\gamma_T g}(\theta)$ observable is then computed using the standard jackknife expressions (Norberg et al. 2009). This approach to measuring the covariance has been validated for $w^{\kappa g}(\theta)$ in Giannantonio et al. (2016). Further tests of the jackknife covariance estimation for $w^{\gamma_T g}(\theta)$ are presented in Clampitt et al. (2016). The maximum angular scale used in this analysis ($\theta_{\rm max} = 50'$) is chosen to be comparable to the size of the jackknife subregions. The correlation matrix, $corr(i,j) = C_{ij}/\sqrt{C_{ii}C_{jj}}$ computed from the jackknife covariance, C_{ij}, is shown in Fig. 5. The observables are ordered as indicated in the figure, with θ increasing to the right.

Fig. 5 shows that $w^{\kappa g}(\theta)$ measurements at different angular scales are significantly correlated. This is primarily due to noise correlations in the κ map, which arise because the two main sources of κ noise—the Gaussian primary CMB fluctuations and noise in the SPT temperature maps—are significantly non-white in the pixel domain. Additionally, the smoothing of the κ maps with a Gaussian beam (see §3.2) increases the correlations between different angular scales. On the other hand, it is clear from the figure that the $w^{\kappa g}(\theta)$ and $w^{\gamma_T g}(\theta)$ measurements are relatively uncorrelated. This is due to the fact that the dominant noise sources in these two observables are uncorrelated. Noise in $w^{\kappa g}(\theta)$ is dom-

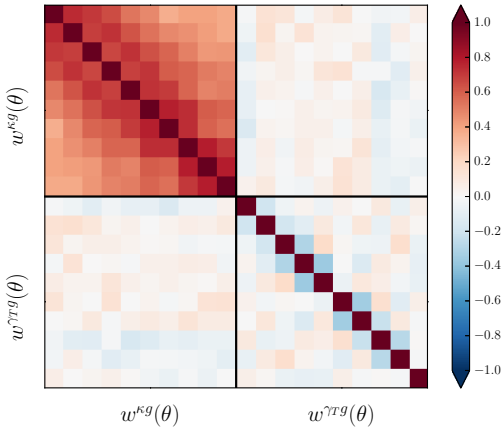

Figure 5. The correlation matrix, $corr(i,j) = C_{ij}/\sqrt{C_{ii}C_{jj}}$, for the joint $w^{\kappa g}(\theta)$ and $w^{\gamma_T g}(\theta)$ observable, where C_{ij} is the covariance matrix element estimate from the jackknife.

inated by noise in the CMB κ map which which receives contributions from both the primary CMB noise and instrumental noise. Noise in the measurement of $w^{\gamma_T g}(\theta)$ is dominated by shape noise at small angular scales, which in turn is uncorrelated with noise in the CMB κ reconstruction.

5 ANALYSIS

5.1 Modeling $w^{\kappa g}(\theta)$ and $w^{\gamma_T g}(\theta)$

We model $w^{\kappa g}(\theta)$ using Eqs. 5 and 6, while $w^{\gamma_T g}(\theta)$ is modeled using Eq. 10. As described in §3.2, the CMB-derived κ map is high-pass filtered to remove modes with $\ell < 30$ and smoothed with a Gaussian beam of $\theta_{\rm FWHM} = 5.4'$. To make our model well-matched to the data, we therefore also apply this same filtering and smoothing to our model for $w^{\kappa g}(\theta)$. To account for the high-pass filtering, we set $C_\ell^{\kappa g} = 0$ for $\ell < 30$ when computing the sum in Eq. 5. To account for the beam smoothing, we multiply each term in the sum in Eq. 5 by $B_\ell^2 = e^{-\ell(\ell+1)\sigma^2}$.

5.1.1 *Bias model*

To fully define our model for the observed lensing cross correlations in Eqs. 5, 6, and 10, we must model both the matter power spectrum, $P(k,\chi)$, and the bias of the tracer galaxies, $b(k,\chi)$. At scales where the matter perturbations are in the linear regime, the power spectrum can be accurately modeled using a Boltzmann code. To this end, we use `CAMB`[6] (Howlett et al. 2012; Lewis et al. 2000). In the nonlinear regime, the matter power spectrum is more difficult to model. A common prescription is `Halofit` (Smith et al. 2003), which calibrates the nonlinear matter power spectrum using dark matter-only N-body simulations. Here we use the updated `Halofit` model from Takahashi et al. (2012). Although `Halofit` has been shown to accurately reproduce the galaxy power spectrum at moderately nonlinear scales (e.g. Crocce et al. 2016), its predictions become more uncertain at still smaller scales where, for instance, baryonic feedback effects may become large (e.g. Jing et al. 2006; van Daalen et al. 2011). At some level, uncertainty in the nonlinear matter power spectrum is incorporated into our analysis through our modeling of the tracer bias, as we discuss in more detail below.

A common approach to parameterizing $b(k,\chi)$ is the so-called linear bias model (Mo & White 1996; Matarrese et al. 1997), for which the bias has no scale dependence, but is allowed to vary with comoving distance: $b(k,\chi) = f(\chi)$. It is well known that the linear bias model accurately describes galaxy clustering over scales where the matter density perturbations are linear, and even at scales several times smaller than the transition scale from the linear to the nonlinear regime (e.g. Crocce et al. 2016). However, at still smaller scales, the simple linear bias model is expected to break down. Since small angular scales contain useful information about the lensing cross-correlations, we would like to use the smallest scale possible for which we can still develop a reasonable bias model. However, we do not know the exact scale at which linear bias remains valid. We therefore take the approach of choosing a range of angular scales for which we believe linear bias to be a reasonable approximation, but introduce additional freedom into our bias model to capture small departures from linear bias. Furthermore, by allowing for freedom in the bias model at small scales, we effectively account for uncertainty in the matter power spectrum at these scales due, for instance, to baryonic effects.

For the benchmark sample used in this work, Crocce et al. (2016) have determined that the linear bias approximation begins to break down at angular scales $\lesssim 3'$ in their measurements of the galaxy auto-correlation at $0.4 < z < 0.6$. We therefore adopt $\theta_{\rm min} = 3'$ in this work. Since Crocce et al. (2016) find that the linear bias approximation is valid at scales smaller than $3'$ for $z > 0.6$, this is a somewhat conservative choice.

We allow for freedom beyond linear bias with a second order Taylor expansion in k and z:

$$b(k,z) = b_0\left[1 + a_1(k/k_0) + a_2(k/k_0)^2\right] \times \left[1 + c_1(z/z_0) + c_2(z/z_0)^2\right], \quad (17)$$

where b_0, a_i and c_i are parameters of the model. Many different approaches to parameterizing the scale dependence (e.g. Bielefeld et al. 2015) and redshift dependence (e.g. Fry 1996; Matarrese et al. 1997; Clerkin et al. 2015) of the bias have been proposed in the literature. Since we are only attempting to capture small deviations from linear bias, a Taylor expansion in k is appropriate here. Our assumed form for the redshift dependence of the bias is simple and flexible. As we show in §6.4, our constraints on the redshift dependence of the bias are weak, so the precise form adopted for this dependence is relatively unimportant to our analysis.

We choose $k_0 = 1\,h\,{\rm Mpc}^{-1}$ for the pivot scale since this is roughly where we expect linear bias to begin breaking down (Crocce et al. 2016), and $z_0 = 0.6$ since this is near the center of the redshift distribution of the tracer galaxies. At $z = 0.6$, $1/k = 1\,h^{-1}{\rm Mpc}$ corresponds to an angular scale of $3.6'$, slightly greater than the minimum angular scale, $\theta_{\rm min} = 3'$. We place flat priors with range $[-5, 5]$ on the bias parameters a_i and c_i; in our analysis we find these priors

[6] `http://camb.info`

are sufficiently wide that they have no effect on any of our constraints.

5.2 Model Parameterizations

Given a cosmological model and the bias model of Eq. 17, we can compute $w^{\kappa g}(\theta)$ and $w^{\gamma_T g}(\theta)$ using the measured $N(z)$ of the tracer and source galaxies. As discussed above, we expect the joint measurement of these two quantities to be sensitive to cosmological parameters, systematics in the lensing measurements, and systematics in the galaxy redshift distributions. We now introduce three model parameterizations that are chosen to explore our sensitivity to these quantities.

5.2.1 Cosmology Analysis

We are interested in the sensitivity of our joint measurement of $w^{\kappa g}(\theta)$ and $w^{\gamma_T g}(\theta)$ to cosmological parameters. As discussed in §2, we expect the joint measurement to be particularly well suited to constraining cosmological parameters that change the geometry or expansion history of the Universe. In the interest of simplicity, we focus on flat ΛCDM cosmological models and explore our ability to constrain Ω_M. All other cosmological parameters are fixed to their best-fit values from a flat-ΛCDM-model fit by Planck Collaboration et al. (2015b) (hereafter PlanckXIII) to their observations of the CMB. These parameter values are $h = 0.6751$, $\Omega_b = 0.0488$, $\tau = 0.063$, $n_S = 0.9653$, and $A_S = 2.1306 \times 10^{-9}$ at a pivot scale of $k = 0.05\,\mathrm{Mpc}^{-1}$, corresponding to $\sigma_8 = 0.815$.

The cosmological analysis considered here is optimistic in the sense that we only vary Ω_M and marginalize over the bias parameters a_i and c_i. A complete cosmological analysis should also marginalize over additional cosmological parameters. Given that our constraints on Ω_M are relatively weak compared to those from PlanckXIII, including the uncertainties on the best-fit cosmological parameters from PlanckXIII would have only a small impact on our results. We remind the reader that the analysis presented here is concerned with early DES SV data and should be viewed as a proof-of-principle work that demonstrates the potential of similar analyses with future DES and SPT data. The cosmological parameterization and the associated priors are summarized in Table 1.

5.2.2 Shear bias parameterization

The joint measurement of $w^{\kappa g}(\theta)$ and $w^{\gamma_T g}(\theta)$ is sensitive to systematics in the measurements of the CMB-derived κ and the galaxy-lensing derived γ_T. We focus on systematics in the γ_T estimates. Systematics affecting the measurement of galaxy shear can result from a number of sources, including incomplete modeling of telescope optics, atmospheric distortion and contamination from nearby sources (J15).

We investigate the ability of the joint $w^{\kappa g}(\theta)$ and $w^{\gamma_T g}(\theta)$ measurement to constrain systematics that scale the absolute calibration of the measured shear, i.e. *multiplicative biases*. We have two reasons for focusing on multiplicative biases and ignoring systematics that additively bias the measured shear. First, as discussed in §4, our measurement of $w^{\gamma_T g}(\theta)$ is expected to be robust to additive shear systematics. Second, joint measurement of $w^{\gamma_T g}(\theta)$ and $w^{\kappa g}(\theta)$ is particularly well suited to constraining multiplicative shear systematics (Vallinotto 2013). If one only measures $w^{\gamma_T g}(\theta)$, the multiplicative systematic will be completely degenerate with the scale-independent tracer bias since both affect the normalization of $w^{\gamma_T g}(\theta)$. Joint measurement with $w^{\kappa g}(\theta)$, however, allows this degeneracy to be broken since $w^{\kappa g}(\theta)$ does not depend on galaxy shear systematics at all.

Typically, systematic errors in galaxy shear measurements are estimated by dividing the full shear catalog into subsamples that are expected to yield consistent shear estimates, but may not because of some systematic effect (e.g. Mandelbaum et al. 2006). The difference between shear estimates from the various subsamples is then reflective of the magnitude of the systematic effect in question. However, these internal consistency tests do not constrain the absolute shear calibration since systematic errors in the calibration will affect all subsamples in the same way. Therefore, to estimate errors on the shear calibration, one often relies on image simulations (e.g. Schrabback et al. 2007; Kacprzak et al. 2012). Image simulations, however, can be problematic if they are not perfectly matched to the datasets in question.

The joint measurement of $w^{\kappa g}(\theta)$ and $w^{\gamma_T g}(\theta)$ considered here can be used to constrain the absolute shear calibration. Multiplicative systematics in the galaxy shears will not affect the CMB lensing measurements, allowing the degeneracy between shear calibration and galaxy bias to be broken in the joint lensing measurement. Therefore, the joint lensing measurement can be used to constrain the absolute shear calibration without resorting to simulations.

Following the convention of Heymans et al. (2006), we parameterize the multiplicative galaxy shear systematic with a single parameter, m, so that the model tangential shear is

$$\gamma_T = (1+m)\gamma_T^{\mathrm{no-sys}}, \tag{18}$$

where $\gamma^{\mathrm{no-sys}}$ is the model shear in the absence of any systematic effect. In the absence of any systematic effect we should recover $m = 0$.

5.2.3 Redshift bias parameterization

We also expect the joint lensing measurement considered here to be sensitive to systematic errors in the photometric redshift estimates of the tracer and source galaxies. Systematics in the photo-z estimates of the tracer galaxies will change the model predictions for both $w^{\kappa g}(\theta)$ and $w^{\gamma_T g}(\theta)$; systematics in the photo-z estimates of the source galaxies will change the predicted $w^{\gamma_T g}(\theta)$, but not the predicted $w^{\kappa g}(\theta)$. Therefore, it should be possible to constrain photo-z systematics in the joint fit to these two lensing-tracer correlations. Taking this reasoning a step further, in principle one could use the joint $w^{\kappa g}(\theta)$ and $w^{\gamma_T g}(\theta)$ measurement to constrain the full $N(z)$ for the tracer or source galaxies. For this first measurement with DES SV data, however, we expect the signal-to-noise to be relatively low. We therefore focus here on constraining a single photo-z systematic parameter rather than the full $N(z)$. Future DES data will make constraining the full $N(z)$ with joint measurement of

$w^{\kappa g}(\theta)$ and $w^{\gamma_T g}(\theta)$ an exciting possibility (see discussion in §7).

It is easiest to gain intuition for the ability of the joint lensing observable to constrain the tracer and source galaxy redshift distributions in the limit that the tracer redshift distribution is narrow and the bias is scale and redshift-independent. In that limit, $w^{\kappa g}(\theta) \propto g^{\rm CMB}(\chi^g) b_0$ and $w^{\gamma_T g}(\theta) \propto g^s(\chi^g) b_0$, where the g-factors are defined in §2, χ^g is the comoving distance of the tracer galaxies, and b_0 is the tracer bias. The measured redshift distributions then enter into the model predictions for $w^{\kappa g}(\theta)$ and $w^{\gamma_T g}(\theta)$ only through $g^{\rm CMB}(\chi^g)$ and $g^s(\chi^g)$. For a single measurement of either $w^{\kappa g}(\theta)$ or $w^{\gamma_T g}(\theta)$, then, b_0 is completely degenerate with the redshift information. The joint lensing cross-correlation measurement, however, breaks this degeneracy because $g^{\rm CMB}(\chi^g)$ and $g^s(\chi^g)$ depend in different ways on the tracer and source redshift distributions.

Photometric redshift estimation is a notoriously difficult problem, and can be affected by a host of different systematic errors (in the context of DES see, for instance, Sánchez et al. 2014). These systematic errors can change the inferred $N(z)$ of both the sources and the tracers in complicated ways. Here, we take a simplistic approach and parameterize only the systematic error in the tracer photometric redshifts with a single parameter, Δ_z, which simply shifts (in redshift) the model $N(z)$ for the tracers:

$$N(z) = \begin{cases} N_{\rm no-sys}(z - \Delta_z), & \text{if } z - \Delta_z > 0 \\ 0, & \text{otherwise,} \end{cases} \tag{19}$$

where $N_{\rm no-sys}(z)$ is the tracer $N(z)$ in the absence of any systematic. Note that we enforce the physical requirement that $N(z) = 0$ for $z < 0$. The treatment adopted here has the advantages of simplicity and generality: any systematic which changes the mean $N(z)$ of the tracers is likely to generate an effective Δ_z, and should therefore be constrained by this analysis. The Dark Energy Survey Collaboration et al. (2015) have adopted the same parameterization of photo-z systematics in the analysis of the cosmic shear two-point function. Note that although we consider only Δ_z for the tracers in this analysis, the joint analysis of $w^{\gamma_T g}(\theta)$ and $w^{\kappa g}(\theta)$ could also be used to constrain Δ_z for the sources. We have chosen to focus on Δ_z for the tracers because the constraint on Δ_z for the sources is quite weak with current data.

5.2.4 *Other sources of systematic error*

Of course, there are many other ways that systematics could affect the joint lensing-galaxy cross-correlation measurements besides those considered above. We focus our analysis on multiplicative shear systematics and photometric redshift systematics because these are likely to be some of the most significant sources of systematic error in the data, and because the joint $w^{\kappa g}(\theta)$ and $w^{\gamma_T g}(\theta)$ measurement is particularly well suited to constraining these systematics.

Crocce et al. (2016) have constrained several different potential sources of systematic error — including variations in observation conditions and stellar and dust contamination — that may impact the distribution of benchmark galaxies and have found that above $z \gtrsim 0.4$, their impact is likely small. Several systematic effects that may affect the SPT κ maps have been considered by van Engelen et al. (2012). These include sources of contamination, such as emissive point sources, the Sunyaev-Zel'dovich effect, and the cosmic infrared background, as well as other effects, such as beam uncertainties. The analysis of van Engelen et al. (2012) indicates that the impact of these sources of systematic error on their measurement of the lensing power spectrum is significantly smaller than the corresponding statistical errorbars, suggesting that such effects likely have a negligible impact on the analysis presented here. Giannantonio et al. (2016) have considered how several different systematics — in both DES and SPT data — may impact the measurement of $w^{\kappa g}(\theta)$, finding no evidence for significant contamination. Finally, we mention that if there is overlap between the source and tracer galaxies in redshift, then intrinsic alignment effects (Troxel & Ishak 2015) can lead to a distinct signature in the measured γ_T that could in principle be constrained using the joint $w^{\kappa g}(\theta)$ and $w^{\gamma_T g}(\theta)$ observable. Since $w^{\gamma_T g}(\theta)$ would be affected by intrinsic alignments while $w^{\kappa g}(\theta)$ is not, the joint lensing observable is a potentially attractive probe of these effects.

5.3 Likelihood

We adopt a Gaussian likelihood for the data given our model vector:

$$\mathcal{L}(\vec{d}|\vec{p}) \propto \exp\left[-\frac{1}{2}\left(\vec{d} - \vec{t}(\vec{p})\right)^T \widehat{\mathbf{C}^{-1}} \left(\vec{d} - \vec{t}(\vec{p})\right)\right], \tag{20}$$

where $\vec{d} = (\hat{w}^{\kappa g}(\vec{\theta}), \hat{w}^{\gamma_T g}(\vec{\theta}))$ is the joint data vector of the CMB and galaxy lensing measurements and $\vec{t}(\vec{p})$ is the model (theory) vector, expressed as a function of the parameter vector, $\vec{p}$. $\widehat{\mathbf{C}^{-1}}$ is our estimator for the inverse covariance matrix of the data vector. Following Hartlap et al. (2007) and Friedrich et al. (2016), we estimate the inverse covariance matrix using

$$\widehat{\mathbf{C}^{-1}} = \frac{N - d - 2}{N - 1}\mathbf{C}^{-1}, \tag{21}$$

where N is the number of jackknife regions (in this case $N = 200$), d is the length of our data vector (in this case $d = 20$) and $\mathbf{C}$ is the covariance matrix estimated from the jackknifing procedure.

We parameterize $\vec{t}(\vec{p})$ as discussed in §5.2.1, §5.2.2, and §5.2.3. For each of these three parameterizations, we hold the parameters in the other two models fixed. For the cosmology analysis this means fixing $m = 0$, and $\Delta_z = 0$. For the shear and redshift systematics analyses, this means fixing the cosmological model to the best fit flat-ΛCDM cosmological model from the CMB only analysis of PlanckXIII and fixing $\Delta_z = 0$ or $m = 0$, respectively. These values (and the other priors imposed on our models) are summarized in Table 1. This approach is motivated by the two main goals of this work. First, we wish to show that the measurements of $w^{\kappa g}(\theta)$ and $w^{\gamma_T g}(\theta)$ are self consistent and that they agree with the currently favored flat-ΛCDM cosmological model. For this purpose, it is sufficient to consider the parameter constraints along particular directions in parameter space. Second, we wish to highlight the potential of the joint $w^{\kappa g}(\theta)$ and $w^{\gamma_T g}(\theta)$ measurements to constrain cosmology, shear systematics and redshift distributions. With current DES SV

data, the constraints that we obtain on the model parameters are weak relative to other published constraints. Treating each model fit separately, then, can be seen as imposing tight (but realistic) external priors on the quantities that are not varied. Finally, the approach adopted here has the advantage of simplicity, appropriate for a first measurement that has low signal-to-noise. For future joint measurements of $w^{\kappa g}(\theta)$ and $w^{\gamma_T g}(\theta)$ that have higher signal-to-noise it may be appropriate to vary all of the model parameters simultaneously.

Given the likelihood of Eq. 20 and the priors discussed above, we can calculate the posterior on our model parameters. We sample the multidimensional posterior using a Markov Chain Monte Carlo approach implemented with the code `emcee` (Foreman-Mackey et al. 2013). Our entire pipeline (from computation of the model vector to sampling of the parameter space) is implemented using `COSMOSIS`[7] (Zuntz et al. 2015).

6 RESULTS

6.1 Measurement and consistency test

Fig. 6 shows our measurements of $w^{\kappa g}(\theta)$ (top panel) and $w^{\gamma_T g}(\theta)$ (bottom panel). The error bars shown are the diagonal elements of the jackknife covariance matrix. Note that the error bars on both the $w^{\kappa g}(\theta)$ and $w^{\gamma_T g}(\theta)$ measurements are correlated between different angular scales, as shown in Fig. 5. The significance of the joint $w^{\kappa g}(\theta)$ and $w^{\gamma_T g}(\theta)$ measurement is roughly 19σ. The solid (purple) curve in Fig. 6 represents the best-fit model from the cosmology analysis discussed in §5.2.1, where Ω_M and the bias parameters b_0, a_i, and c_i are allowed to vary. Note that this curve represents a *joint* fit to the $w^{\kappa g}(\theta)$ and $w^{\gamma_T g}(\theta)$ measurements; in other words, the same parameters define the model curves in both the top and bottom panels. The dashed (green) curve in Fig. 6 represents the best-fit model when we fix $\Omega_M = 0.3121$ (i.e. the best fit value from a flat-ΛCDM fit to CMB observations in PlanckXIII) and $a_i = c_i = 0$, but allow b_0 to vary. Both model curves agree well with the data, and neither model is strongly preferred over the other (as we quantify in more detail below). The dotted (black) curve in Fig. 6 corresponds to $w^{\kappa g}(\theta) = 0$.

As a consistency check on the data, we first perform fits to the $w^{\kappa g}(\theta)$ and $w^{\gamma_T g}(\theta)$ measurements separately (i.e. *not* jointly) in which the cosmological model is fixed to the best fit flat-ΛCDM model from the analysis of CMB data by PlanckXIII, while the redshift-independent bias coefficient, b_0, is allowed to vary and $a_i = c_i = 0$. These fits are not the primary focus of this work (because they treat the $w^{\kappa g}(\theta)$ and $w^{\gamma_T g}(\theta)$ measurements separately and because they assume constant bias down to the smallest angular scales that we measure) but they allow us check the SPT and DES data for consistency, and also to compare how constraining these two data sets are. From the analysis of $w^{\kappa g}(\theta)$, we find $b_0 = 1.14 \pm 0.31$; from the analysis of $w^{\gamma_T g}(\theta)$ we find $b_0 = 1.26 \pm 0.07$. Making the assumption that the errors on the $w^{\kappa g}(\theta)$ and $w^{\gamma_T g}(\theta)$ measurements are uncorrelated (a reasonable assumption given Fig. 5), these two b_0 constraints are consistent at roughly 0.4σ. However, the constraints on b_0 from $w^{\gamma_T g}(\theta)$ are tighter than those from $w^{\kappa g}(\theta)$ by roughly a factor of 4.6. This is because the error bars on $w^{\kappa g}(\theta)$ are larger and more correlated than the error bars on $w^{\gamma_T g}(\theta)$. The tightness of the joint constraint on b_0 suggests that we may be able to measure variation of the bias with redshift; this possibility is explored more in §6.4.

The constraints on b_0 obtained above are also consistent with the results of other analyses of DES SV data. Our measurement of b_0 from SPT data is consistent with the measurements of Giannantonio et al. (2016), which also measured $w^{\kappa g}(\theta)$ using a similar catalog of benchmark galaxies and identical CMB κ maps. Giannantonio et al. (2016) found best fit constant biases of $b_0 = 0.75 \pm 0.25$ and $b_0 = 1.25 \pm 0.25$ for the redshift bins $z \in [0.4, 0.6]$ and $z \in [0.6, 0.8]$, respectively. Averaging these two measurements yields a bias of $b_0 \sim 1.0$, consistent with our measurement of b_0 using $w^{\kappa g}(\theta)$ within the error bars. A quantitative comparison to Giannantonio et al. (2016) is difficult because we use an identical CMB-κ map, but somewhat different versions of the benchmark catalog (and mask) and a different photometric redshift estimation code.

Our measurement of b_0 is also consistent with constraints on b_0 obtained by Crocce et al. (2016) from measuring galaxy clustering of the benchmark galaxy sample. Using the TPZ photometric redshift algorithm (Carrasco Kind & Brunner 2013, 2014), Crocce et al. (2016) found best fit constant bias parameters $b_0 = 1.29 \pm 0.04$ and $b_0 = 1.34 \pm 0.05$ for the redshift bins $z \in [0.4, 0.6]$ and $z \in [0.6, 0.8]$, respectively. These two measurements yield an average bias of $b_0 \sim 1.32$, which is consistent with the constraints we obtain from $w^{\kappa g}(\theta)$ and $w^{\gamma_T g}(\theta)$ to within the error bars. Again, a quantitative comparison to Crocce et al. (2016) is difficult because we use a slightly different benchmark catalog and a different photometric redshift estimation code.

6.2 Bias degeneracies

To gain intuition for how the joint $w^{\kappa g}(\theta)$ and $w^{\gamma_T g}(\theta)$ measurement breaks degeneracies with tracer bias, we now present constraints in the two dimensional plane defined by b_0 and each of the three model parameters defined in §5.2.1, §5.2.2, and §5.2.3. For this analysis, we fix the bias parameters $a_i = c_i = 0$, which corresponds to a constant bias model described by b_0 alone; doing so considerably simplifies the interpretation and visualization of the results. However, as noted previously, we expect that constant bias may not accurately describe the data at small angular separations. We therefore restrict the analysis presented in this section to angular scales $\theta > 10'$, which should be safely in the linear bias regime (Crocce et al. 2016). Imposing this restriction on the data will weaken our constraints, but we remind the reader that our intent in this section is only to gain intuition for degeneracies with b_0. In §6.3 we will present results that use data at small angular scales and for which we allow the bias parameters a_i and c_i to vary.

The leftmost panel of Fig. 7 presents the constraints obtained from the analysis of $w^{\kappa g}(\theta)$ and $w^{\gamma_T g}(\theta)$ in the Ω_M–b_0 plane. Each shaded region corresponds to a contour of the posterior probability such that the $\Delta\chi^2$ relative to the min-

[7] https://bitbucket.org/joezuntz/cosmosis/wiki/Home

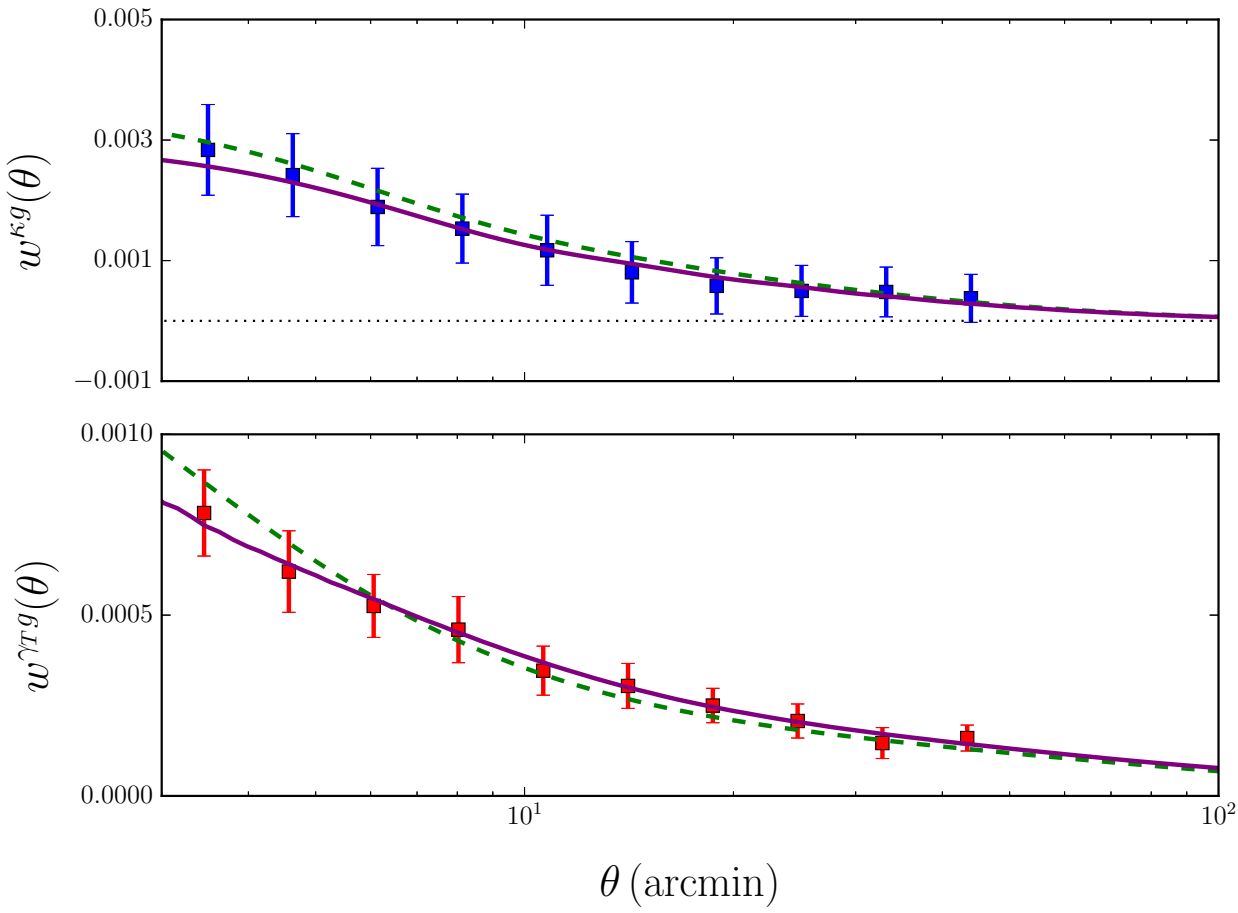

Figure 6. The measured $w^{\kappa g}(\theta)$ (top panel) and $w^{\gamma_T g}(\theta)$ (bottom panel). Error bars are the square roots of the diagonal elements of the covariance matrix. Solid (purple) curve shows the best-fit model using the parameterization discussed in §5.2.1, for which Ω_M and b_0, a_i and c_i are free parameters. Dashed (green) curve shows the best-fit model when only b_0 is allowed to vary, $a_i = c_i = 0$, and the cosmological parameters are fixed to the best-fit flat-ΛCDM model from the CMB-only analysis of PlanckXIII. Both model curves result from *joint* fits to the $w^{\kappa g}(\theta)$ and $w^{\gamma_T g}(\theta)$ measurements. The dotted line in the top panel shows $w^{\kappa g}(\theta) = 0$.

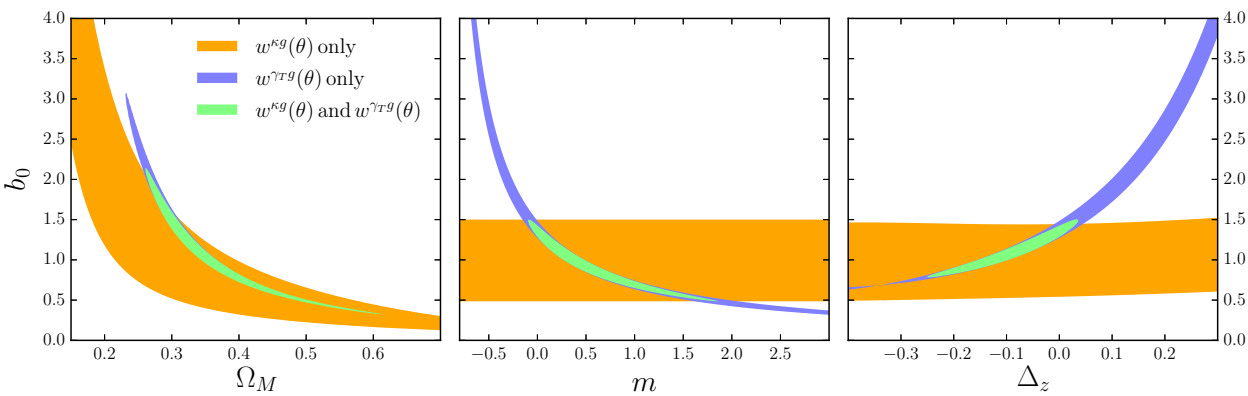

Figure 7. Constraints obtained on the three model parameters when we fix the bias parameters $a_i = c_i = 0$, but allow b_0 to vary; contours show where $\Delta\chi^2 = 1$ relative to the minimum χ^2. Orange contour shows the constraint obtained from analysis of $w^{\kappa g}(\theta)$ alone; blue contour shows the constraint obtained from analysis of $w^{\gamma_T g}(\theta)$ alone; green contour shows the constraint obtained from the joint analysis of $w^{\kappa g}(\theta)$ and $w^{\gamma_T g}(\theta)$. In all cases, the joint measurement of $w^{\kappa g}(\theta)$ and $w^{\gamma_T g}(\theta)$ helps to break degeneracies between the model parameters of interest and the bias parameter b_0. We have restricted the analysis here to angular scales $\theta > 10'$ to ensure that linear bias remains valid.

imum is $\Delta\chi^2 = 1$ (this value of $\Delta\chi^2$ was chosen to improve the visualization since the constraints obtained in this analysis are fairly weak owing to the exclusion of the small angle measurements). The orange region shows the constraints obtained from analysis of $w^{\kappa g}(\theta)$ alone; the blue region shows the constraints obtained from analysis of $w^{\gamma_T g}(\theta)$ alone; the green region shows the constraints obtained from the joint analysis of $w^{\kappa g}(\theta)$ and $w^{\gamma_T g}(\theta)$. Since there is little covariance between $w^{\kappa g}(\theta)$ and $w^{\gamma_T g}(\theta)$, the joint constraints are roughly the product of the individual constraints. From the figure it is clear that there is a strong degeneracy between Ω_M and b_0 for both $w^{\kappa g}(\theta)$ and $w^{\gamma_T g}(\theta)$. The joint measurement of both $w^{\kappa g}(\theta)$ and $w^{\gamma_T g}(\theta)$ helps to break this degeneracy.

The middle panel of Fig. 7 shows the constraints obtained from the analysis of $w^{\kappa g}(\theta)$ and $w^{\gamma_T g}(\theta)$ in the m–b_0 plane. Since $w^{\kappa g}(\theta)$ does not depend at all on m, we obtain no constraint on m from the analysis of $w^{\kappa g}(\theta)$ alone (orange region). $w^{\gamma_T g}(\theta)$ depends on m, but in a way that is completely degenerate with b_0 (blue region); we therefore also obtain no constraint on m from $w^{\gamma_T g}(\theta)$ alone. The joint measurement of $w^{\kappa g}(\theta)$ and $w^{\gamma_T g}(\theta)$, however, breaks this degeneracy with the bias as shown by green region.

The rightmost panel of Fig. 7 shows the constraints obtained from the analysis of $w^{\kappa g}(\theta)$ and $w^{\gamma_T g}(\theta)$ in the Δ_z–b_0 plane. Changing Δ_z does not have a very large impact on $w^{\kappa g}(\theta)$ because the CMB source plane is at much higher redshift than the tracer galaxies; any reasonable Δ_z is very small compared to the redshift of the surface of last scattering. This fact combined with the low signal-to-noise of the $w^{\kappa g}(\theta)$ measurement means that we do not obtain a constraint on Δ_z from $w^{\kappa g}(\theta)$ alone (orange region). Furthermore, because the constraint obtained from $w^{\gamma_T g}(\theta)$ alone is highly degenerate with b_0, we also do not obtain a constraint on Δ_z from $w^{\gamma_T g}(\theta)$ alone (blue region). The joint measurement of $w^{\kappa g}(\theta)$ and $w^{\gamma_T g}(\theta)$, however, breaks the degeneracy between Δ_z and b_0 (green region).

It is also interesting to note the direction of the degeneracy between between Δ_z and b_0. For the constraints obtained from $w^{\gamma_T g}(\theta)$, there is a clear positive correlation between Δ_z and b_0. This is because increasing Δ_z for the tracer galaxies pushes $W^g(z)$ to higher redshift. At high redshift, $g^s(z)$ is reduced and $P(k,z)$ is also reduced because of the growth of structure. These two effects lead to a lower $w^{\gamma_T g}(\theta)$, which is offset by increasing b_0. The net result is a positive correlation between Δ_z and b_0. Somewhat suprisingly, there is also a very slight positive correlation between Δ_z and b_0 for the constraints obtained from $w^{\kappa g}(\theta)$. This slight correlation is due to two competing effects: $g^{\rm CMB}(z)$ increases with redshift while $P(k,z)$ decreases with redshift. For our particular tracer galaxy sample, the effect of $P(k,z)$ decreasing with redshift dominates over the effect of $g^{\rm CMB}(z)$ decreasing with redshift. The net result is that $w^{\kappa g}(\theta)$ decreases slightly with Δ_z, leading to a weak correlation between Δ_z and b_0.

6.3 Bias-marginalized parameter constraints

The results presented in §6.2 were restricted to constant bias (i.e. $a_i = c_i = 0$) and for this reason used only the correlation function measurements at large angular scales ($\theta > 10'$). As we have argued in §5.1.1, by allowing additional freedom in our bias model, we can use measurements at smaller angular scales and thereby increase our signal-to-noise without worrying about biasing our results. We now present the constraints obtained when we allow a_i and c_i to vary in our model fits (we refer to this as the *evolving bias* analysis). For these results, we marginalize over all the bias parameters (b_0, a_i and c_i), showing only the posteriors on the model parameters of interest. The posteriors for the three analyses of §5.2.1, §5.2.2, and §5.2.3 are shown as the solid (red) curves in Fig. 8. For comparison, we also show the posteriors on model parameters for the constant bias analysis with $a_i = c_i = 0$ (dashed blue curves). Both the evolving bias and the constant bias curves shown in Fig. 8 were obtained using the $w^{\kappa g}(\theta)$ and $w^{\gamma_T g}(\theta)$ measurements across the full angular range shown in Fig. 6.

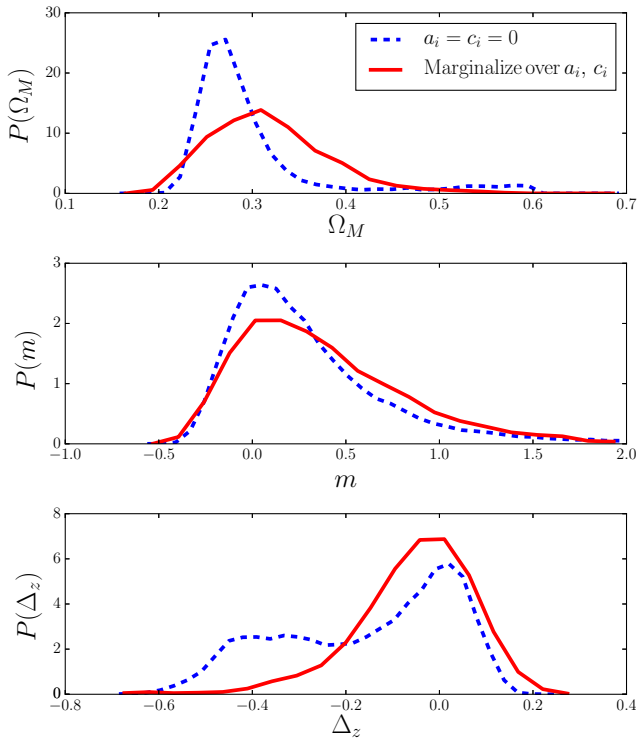

Figure 8. Posteriors on the main parameters of the three models discussed in §5. Solid (red) curves show the results when we marginalize over the bias parameters a_i and c_i. Dashed (blue) curves show the result when we fix $a_i = c_i = 0$. The three analyses are consistent with the best-fit ΛCDM model from PlanckXIII and with no systematic contamination of the shear or photo-z measurements.

The top panel of Fig. 8 shows the posteriors on Ω_M resulting from the analysis described in §5.2.1. The 68% posterior interval on Ω_M from the evolving bias analysis is $(0.26, 0.39)$, while the posterior from the constant bias analysis is $(0.25, 0.33)$. Both of these intervals contain the best-fit value of $\Omega_M = 0.3121$ from the CMB-only analysis of PlanckXIII. The constraints from the constant and evolving bias analyses are also consistent with each other, although the constraint from the evolving bias analysis is weaker. The consistency of the results from the two different bias parameterizations suggests that there is no strong

evidence for departures from linear bias; we quantify this statement in more detail in §6.4.

Note that our roughly 20% constraint on Ω_M uses only $\sim$ 3% of full survey DES Data. With more data, we expect the constraints on $w^{\kappa g}(\theta)$ and $w^{\gamma_T g}(\theta)$ to tighten significantly. This measurement with early DES SV and SPT data indicates that the data are in good agreement with each other and with the best fit cosmological model from PlanckXIII. We refrain from comparing our constraint on Ω_M to other published constraints because we have (intentionally) not performed a complete cosmological analysis here.

The middle panel of Fig. 8 shows the posterior on m — the multiplicative shear systematic parameter — in the evolving bias parameterization. The dashed (blue) curve shows the posterior on m for the constant bias parameterization. The 68% posterior interval on m is $(-0.05, 0.80)$ in the evolving bias parameterization and $(-0.07, 0.68)$ in the constant bias parameterization. Both of these intervals contain $m = 0$ and are therefore consistent with no systematic bias of the galaxy shear measurements. However, both posteriors on m are highly non-Gaussian, exhibiting longs tail to quite large values of m.

It is interesting to note that unlike the constraints on Ω_M, the constraints on m appear to be fairly robust to marginalization over the evolving bias parameters. This behavior can be understood as follows. Information about Ω_M comes from both the relative amplitudes of $w^{\kappa g}(\theta)$ and $w^{\gamma_T g}(\theta)$ (i.e. the lensing ratio of Das & Spergel 2009) as well as the shape of the two correlation functions. Marginalization over the evolving bias parameters effectively washes out some of the information content in the shapes of the correlation functions by allowing the shapes to vary. Therefore, it is not surprising that we find some degradation in the Ω_M constraints with marginalization over the evolving bias parameters. On the other hand, all of the information about m comes from the relative amplitudes of $w^{\kappa g}(\theta)$ and $w^{\gamma_T g}(\theta)$ since m simply scales these two functions relative to each other. Consequently, allowing the shape of the correlation functions to vary by marginalizing over the evolving bias parameters does not have a significant impact on the m constraints since the relative amplitude information is preserved.

J15 used image simulations and a comparison of two shear pipelines to constrain the multiplicative shear systematic parameter to be $|m| \lesssim 0.05$. The constraint on m obtained here is asymmetric around $m = 0$ so it is somewhat difficult to compare directly to the constraint obtained in J15. The lower limit of our 68% posterior interval in the evolving bias analysis (-0.05) is roughly that obtained in J15. However, the upper limit of our 68% confidence interval (0.80) is considerably weaker than that obtained in J15. The width of our constraint on m is roughly a factor of 8 larger than that of J15. Note, though, that the constraint on m presented here relies only on the data, in contrast to the simulation-based approach of J15. We discuss prospects for improvement of the constraint on m in §7.

The bottom panel of Fig. 8 shows the constraints on Δ_z — the systematic error parameter describing a shift in the photometrically measured tracer galaxy $N(z)$ — in the evolving bias analysis. The dashed (blue) curve shows the constraint on Δ_z for the constant bias analysis. The 68% posterior interval on Δ_z in the evolving bias analysis is $(-0.17, 0.07)$ while it is $(-0.38, 0.04)$ for the constant bias analysis. Both of these intervals contain $\Delta_z = 0$, and are therefore consistent with no systematic bias of the tracer galaxy $N(z)$. Our constraints on Δ_z are consistent with the analysis of Bonnett et al. (2015), which compared `skynet2` photo-z estimates to spectroscopically measured redshifts. Bonnett et al. (2015) found that difference between the mean photo-z and the mean spectroscopic redshift was less than ~ 0.04 for galaxies in the DES SV 'Gold' catalog.

It is a bit surprising that marginalization over the evolving bias parameters causes the constraint on Δ_z to tighten slightly. The explanation for this behavior can be deduced from Fig. 8. The posterior on Δ_z in the constant bias model case exhibits two peaks, the larger centered at $\Delta_z \approx 0$ and the smaller at $\Delta_z \approx -0.4$. The two peaks in the posterior result from weak tension between the $w^{\gamma_T g}(\theta)$ and $w^{\kappa g}(\theta)$ measurements in the constant bias model for the fiducial cosmological parameters. Marginalization over the evolving bias parameters allows the shape of $w^{\kappa g}(\theta)$ and $w^{\gamma_T g}(\theta)$ to vary somewhat, relieving this tension and causing the posterior to prefer $\Delta_z \approx 0$. So by effectively excluding the peak at $\Delta_z \approx -0.4$, the posterior that marginalizes over a_i and c_i has lower variance than the posterior that keeps $a_i = c_i = 0$. We emphasize that the tension between $w^{\kappa g}(\theta)$ and $w^{\gamma_T g}(\theta)$ is weak and that it is only relevant to the constant bias analysis (which is not expected to be a very good match to the data anyway).

Although our constraint on Δ_z is weaker than those of Bonnett et al. (2015) by a factor of a few, it was obtained without the need for any spectroscopic calibration sample and used only $\sim$ 3% of the full DES survey area. In many ways, this is one of the most exciting results of this work: we have shown the photo-z distribution can be tightly constrained using the joint measurement of $w^{\kappa g}(\theta)$ and $w^{\gamma_T g}(\theta)$. The measurement presented here serves as a test case for future applications of this potentially powerful technique for estimating galaxy redshift distributions.

6.4 Effects of bias parameter marginalization

The results shown as the solid (red) curves in Fig. 8 were obtained from model fits that allowed the bias parameters a_i and c_i to vary, while the dashed (blue) curves show the posteriors on our model parameters for the constant bias analysis, i.e. when we fix $a_i = c_i = 0$. Since the a_i affect the model prediction at small angular scales, marginalization over these parameters effectively down-weights the contribution of small scales to the likelihood. It is clear from Fig. 8 that the evolving bias marginalization has a fairly small effect on our results.

Rather than marginalizing over b_0, a_i, and c_i, it is also possible to consider the constraints on these parameters from the analysis of $w^{\kappa g}(\theta)$ and $w^{\gamma_T g}(\theta)$. Constraints on these three bias parameters translate into constraints on $b(k, z)$, and these constraints are presented in Fig. 9. To generate this figure, we drew b_0, a_i and c_i from the Markov Chains of the cosmology analysis (the results of the other analyses look similar). Using these parameter values, we then evaluated the resultant $b(k, z)$ across a range of k (top panel) and z (bottom panel) values and the 68% confidence band on

Table 1. Priors and posteriors on the model parameters introduced in §5.2.1, §5.2.2, and §5.2.3. The three different analyses (*cosmology*, *shear calibration*, and *tracer redshift*) are each aimed at constraining a different parameter (Ω_M, m, and Δ_z); the posteriors on these parameters are shown in the last two columns. The *constant bias* column corresponds to letting the bias parameter b_0 vary, but fixing $a_i = c_i = 0$; the *evolving bias* column corresponds to letting b_0, a_i and c_i vary simultaneously. All cosmological parameters not shown in the table are fixed to their best fit values from the CMB-only analysis of PlanckXIII.

Analysis Name	Ω_M	Δ_z	m	68% posterior interval, constant bias	68% posterior interval, evolving bias
Cosmology	$[0.05, 0.6]$	0.0	0.0	$\Omega_M \in (0.25, 0.33)$	$\Omega_M \in (0.26, 0.38)$
Shear calibration	0.3121	0.0	[-3.0, 4.0]	$m \in (-0.07, 0.68)$	$m \in (-0.05, 0.80)$
Tracer redshift	0.3121	[-0.5, 0.5]	0.0	$\Delta_z \in (-0.38, 0.04)$	$\Delta_z \in (-0.17, 0.07)$

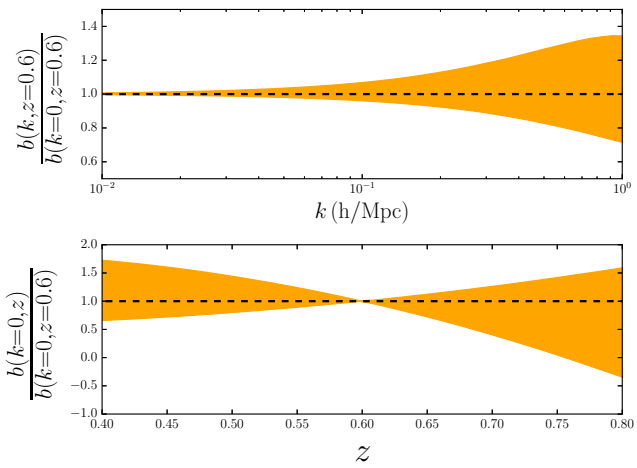

Figure 9. 68% confidence bands on the bias model $b(k, z)$ (Eq. 17) resulting from the cosmology analysis discussed in §5.2.1. In this analysis, we vary Ω_M and the bias parameters b_0, a_i and c_i. The bias models shown are normalized by $b(k = 0, z = 0.6)$ for clarity. The data are consistent with no evolution of the bias in k and z.

$b(k, z)$ was determined. We have normalized the results in both panels of Fig. 9 by the large-scale (i.e. $k = 0$) bias at $z = 0.6$ (roughly the center of the redshift distribution for the tracer galaxies). Fig. 9 shows that at 68% confidence, there is no evidence for departures from constant bias (i.e. $a_i = c_i = 0$).

7 DISCUSSION

We have presented a joint measurement of galaxy-galaxy lensing and galaxy-CMB lensing using DES SV imaging data and CMB lensing data from the SPT-SZ survey. The measurements of $w^{\kappa g}(\theta)$ and $w^{\gamma_T g}(\theta)$ presented here are in agreement with other recent analyses of DES SV data (Giannantonio et al. 2016; Crocce et al. 2016; Clampitt et al. 2016). We have performed fits to the joint measurement of $w^{\kappa g}(\theta)$ and $w^{\gamma_T g}(\theta)$ to extract constraints on cosmology and the presence of systematics in the data. In general, these fits illustrate that data from SPT and DES are in good agreement with each other in the framework of the currently favored flat-ΛCDM cosmological model from PlanckXIII.

Assuming cosmology is well-constrained by other datasets, we have shown that the joint measurement of $w^{\kappa g}(\theta)$ and $w^{\gamma_T g}(\theta)$ can be used to constrain shear calibration as well as galaxy redshift distributions, $N(z)$. The constraints obtained on shear calibration in this analysis have the advantage that they do not rely on simulations of the shear measurement process. The constraints obtained on $N(z)$ have the advantage that they do not rely on spectroscopic redshift measurements. Encouragingly, our analysis shows no strong evidence for systematics in either DES shear or photo-z measurements.

Additional data from DES will significantly improve the constraining power of the joint lensing measurement presented here. This analysis used only data from the DES Science Verification region, a small fraction (roughly 3%) of the full survey area. With additional DES imaging, the region of useful overlap between DES and SPT will expand significantly. Ultimately, the overlap between the two surveys is expected to be ~ 2500 sq. deg., roughly 19 times larger than the DES SV area. Approximately, then, the constraints on cosmology and systematics parameters obtained in this work can be expected to tighten by a factor of $\sqrt{19} \sim 4.4$. The improvement is likely to be better than a factor 4.4 since the larger area of SPT and DES overlap will also mean that the measurement of $w^{\kappa g}(\theta)$ and $w^{\gamma_T g}(\theta)$ can be extended to larger angular scales. In this work we set $\theta_{\rm max} = 50'$ to ensure that the maximum angular scale probed was comparable to the size of the jackknife subregions. With larger area, the size of the jackknife subregions can be increased, allowing $\theta_{\rm max}$ to be increased as well. Since there is additional signal at $\theta > 50'$, increasing $\theta_{\rm max}$ will improve parameter constraints. Additionally, using full sky CMB κ maps from Planck (Planck Collaboration et al. 2015a), it will be possible to exploit the full 5000 sq. deg. area of the full DES survey area. This represents a factor of two increase over the SPT and DES overlap, albeit at somewhat lower signal to noise. Below, however, we take a conservative approach and assume only a factor of 4.4 improvement in the signal-to-noise with the final DES data set.

For the cosmology analysis, a factor of 4.4 improvement in the signal-to-noise would result in $\delta\Omega_M \sim 0.009$, comparable to the current error bar on Ω_M from the CMB-only analysis of PlanckXIII. Note, though, that this is not really a fair comparison since our constraint on Ω_M was derived after marginalizing over only the galaxy bias parameters, while the PlanckXIII constraint marginalizes over all the other ΛCDM parameters. Still, there is reason to be optimistic: as shown in Das & Spergel (2009), the ratio $C_\ell^{\kappa_{\rm Gal} g}/C_\ell^{\kappa_{\rm CMB} g}$ does not depend on the galaxy power specrum. While the joint $w^{\kappa g}(\theta)$ and $w^{\gamma_T g}(\theta)$ observable considered here does not exactly share this property, we expect the joint lensing observable to be fairly robust to cosmological parameters that change the shape of the galaxy power spectrum, but that do not change the purely geometrical fac-

tor $g^{\rm CMB}(\chi^g)/g^s(\chi^g)$. A full cosmological analysis is needed to quantify exactly how much marginalization over additional cosmological parameters will degrade our constraint on Ω_M and is beyond the scope of this work. We also note that the constraints on cosmology could be improved further by dividing the tracer and source galaxies into more redshift bins.

A factor of 4.4 tightening of our constraint on the multiplicative shear bias, m, would yield $\delta m \sim 0.1$. This is a factor of two larger than the current constraints of $|m| \lesssim 0.05$ from the analysis presented in J15. Given this result, it is likely that shear calibration will continue to be performed using image simulations. That said, data-only analyses like that considered here have a valuable roll to play as consistency checks on such simulations. Futhermore, future CMB data (see below) could significantly improve the constraints on m obtained with a joint $w^{\kappa g}(\theta)$ and $w^{\gamma_T g}(\theta)$ analysis, making these constraints competitive with simulation calibration.

Tightening our constraint on Δ_z by a factor of 4.4 would result in $\delta(\Delta_z) \sim 0.02$. This is roughly a factor of two tighter than the constraint on Δ_z presented in Bonnett et al. (2015). Joint measurement of $w^{\kappa g}(\theta)$ and $w^{\gamma_T g}(\theta)$ has the potential to be a highly competitive probe of photo-z systematics. Note that our Δ_z analysis was optimistic in the sense that we did not vary m and Δ_z simultaneously, and these two systematics parameters are expected to be somewhat degenerate. However, given tight priors on m from image simulations, the constraints on Δ_z will not be significantly degraded by marginalizing over m.

Future CMB lensing maps from SPT-3G (Benson et al. 2014) and Advanced ACTPol (Calabrese et al. 2014) will significantly improve the signal-to-noise of the CMB lensing measurements. Since the CMB lensing map used here is noise dominated at all but the largest angular scales, future CMB lensing maps obtained with these experiments will improve the signal-to-noise of the joint $w^{\kappa g}(\theta)$ and $w^{\gamma_T g}(\theta)$ measurement beyond the factor of 4.4 considered above. Such future measurements will be able to place interesting constraints on cosmology as well as provide independent checks on the presence of systematic errors in the data using the joint measurement of $w^{\kappa g}(\theta)$ and $w^{\gamma_T g}(\theta)$.

ACKNOWLEDGEMENTS

This paper has gone through internal review by the DES collaboration.

Funding for the DES Projects has been provided by the U.S. Department of Energy, the U.S. National Science Foundation, the Ministry of Science and Education of Spain, the Science and Technology Facilities Council of the United Kingdom, the Higher Education Funding Council for England, the National Center for Supercomputing Applications at the University of Illinois at Urbana-Champaign, the Kavli Institute of Cosmological Physics at the University of Chicago, the Center for Cosmology and Astro-Particle Physics at the Ohio State University, the Mitchell Institute for Fundamental Physics and Astronomy at Texas A&M University, Financiadora de Estudos e Projetos, Fundação Carlos Chagas Filho de Amparo à Pesquisa do Estado do Rio de Janeiro, Conselho Nacional de Desenvolvimento Científico e Tecnológico and the Ministério da Ciência, Tecnologia e Inovação, the Deutsche Forschungsgemeinschaft and the Collaborating Institutions in the Dark Energy Survey.

The Collaborating Institutions are Argonne National Laboratory, the University of California at Santa Cruz, the University of Cambridge, Centro de Investigaciones Energéticas, Medioambientales y Tecnológicas-Madrid, the University of Chicago, University College London, the DES-Brazil Consortium, the University of Edinburgh, the Eidgenössische Technische Hochschule (ETH) Zürich, Fermi National Accelerator Laboratory, the University of Illinois at Urbana-Champaign, the Institut de Ciències de l'Espai (IEEC/CSIC), the Institut de Física d'Altes Energies, Lawrence Berkeley National Laboratory, the Ludwig-Maximilians Universität München and the associated Excellence Cluster Universe, the University of Michigan, the National Optical Astronomy Observatory, the University of Nottingham, The Ohio State University, the University of Pennsylvania, the University of Portsmouth, SLAC National Accelerator Laboratory, Stanford University, the University of Sussex, Texas A&M University, and the OzDES Membership Consortium.

The DES data management system is supported by the National Science Foundation under Grant Number AST-1138766. The DES participants from Spanish institutions are partially supported by MINECO under grants AYA2012-39559, ESP2013-48274, FPA2013-47986, and Centro de Excelencia Severo Ochoa SEV-2012-0234. Research leading to these results has received funding from the European Research Council under the European Union's Seventh Framework Programme (FP7/2007-2013) including ERC grant agreements 240672, 291329, and 306478.

We are grateful for the extraordinary contributions of our CTIO colleagues and the DECam Construction, Commissioning and Science Verification teams in achieving the excellent instrument and telescope conditions that have made this work possible. The success of this project also relies critically on the expertise and dedication of the DES Data Management group.

The South Pole Telescope program is supported by the National Science Foundation through grant PLR-1248097. Partial support is also provided by the NSF Physics Frontier Center grant PHY-0114422 to the Kavli Institute of Cosmological Physics at the University of Chicago, the Kavli Foundation, and the Gordon and Betty Moore Foundation through Grant GBMF#947 to the University of Chicago.

Argonne National Laboratory's work was supported under the U.S. Department of Energy contract DE-AC02-06CH11357.

REFERENCES

Bacon D. J., Refregier A. R., Ellis R. S., 2000, MNRAS, 318, 625

Bartelmann M., 2010, Classical and Quantum Gravity, 27, 233001

Benson B. A., et al., 2014, in Society of Photo-Optical Instrumentation Engineers (SPIE) Conference Series. p. 1 (arXiv:1407.2973), doi:10.1117/12.2057305

Bertin E., Arnouts S., 1996, A&AS, 117, 393

Bielefeld J., Huterer D., Linder E. V., 2015, J. Cosmology Astropart. Phys., 5, 23

Bonnett C., et al., 2015, preprint, (arXiv:1507.05909)

Brainerd T. G., Blandford R. D., Smail I., 1996, ApJ, 466, 623

Calabrese E., et al., 2014, J. Cosmology Astropart. Phys., 8, 10
Carlstrom J. E., et al., 2011, PASP, 123, 568
Carrasco Kind M., Brunner R. J., 2013, MNRAS, 432, 1483
Carrasco Kind M., Brunner R. J., 2014, MNRAS, 442, 3380
Clampitt J., et al., 2016, preprint, (arXiv:1603.05790)
Clerkin L., Kirk D., Lahav O., Abdalla F. B., Gaztañaga E., 2015, MNRAS, 448, 1389
Crocce M., et al., 2016, MNRAS, 455, 4301
Das S., Spergel D. N., 2009, Phys. Rev. D, 79, 043509
Das S., Errard J., Spergel D., 2013, preprint, (arXiv:1311.2338)
Desai S., et al., 2012, ApJ, 757, 83
Foreman-Mackey D., Hogg D. W., Lang D., Goodman J., 2013, PASP, 125, 306
Friedrich O., Seitz S., Eifler T. F., Gruen D., 2016, MNRAS, 456, 2662
Fry J. N., 1996, ApJ, 461, L65
Giannantonio T., et al., 2016, MNRAS, 456, 3213
Górski K. M., Hivon E., Banday A. J., Wandelt B. D., Hansen F. K., Reinecke M., Bartelmann M., 2005, ApJ, 622, 759
Graff P., Feroz F., Hobson M. P., Lasenby A., 2014, MNRAS, 441, 1741
Guzik J., Seljak U., 2001, MNRAS, 321, 439
Hartlap J., Simon P., Schneider P., 2007, A&A, 464, 399
Heymans C., et al., 2006, MNRAS, 368, 1323
Hildebrandt H., et al., 2010, A&A, 523, A31
Howlett C., Lewis A., Hall A., Challinor A., 2012, J. Cosmology Astropart. Phys., 4, 27
Hu W., 2001, ApJ, 557, L79
Hu W., Okamoto T., 2002, ApJ, 574, 566
Hu W., Holz D. E., Vale C., 2007, Phys. Rev. D, 76, 127301
Jain B., Taylor A., 2003, Physical Review Letters, 91, 141302
Jarvis M., Bernstein G., Jain B., 2004, MNRAS, 352, 338
Jarvis M., et al., 2015, preprint, (arXiv:1507.05603)
Jing Y. P., Zhang P., Lin W. P., Gao L., Springel V., 2006, ApJ, 640, L119
Kacprzak T., Zuntz J., Rowe B., Bridle S., Refregier A., Amara A., Voigt L., Hirsch M., 2012, MNRAS, 427, 2711
Kaiser N., 1992, ApJ, 388, 272
Kaiser N., Wilson G., Luppino G. A., 2000, ArXiv Astrophysics e-prints,
Kirk D., et al., 2015, preprint, (arXiv:1512.04535)
Lewis A., Challinor A., Lasenby A., 2000, ApJ, 538, 473
Limber D. N., 1953, ApJ, 117, 134
Liu J., Ortiz-Vazquez A., Hill J. C., 2016, preprint, (arXiv:1601.05720)
Mandelbaum R., Seljak U., Cool R. J., Blanton M., Hirata C. M., Brinkmann J., 2006, MNRAS, 372, 758
Matarrese S., Coles P., Lucchin F., Moscardini L., 1997, MNRAS, 286, 115
Mo H. J., White S. D. M., 1996, MNRAS, 282, 347
Mohr J. J., et al., 2012, in Society of Photo-Optical Instrumentation Engineers (SPIE) Conference Series. p. 0 (arXiv:1207.3189), doi:10.1117/12.926785
Norberg P., Baugh C. M., Gaztañaga E., Croton D. J., 2009, MNRAS, 396, 19
Planck Collaboration et al., 2015b, preprint, (arXiv:1502.01589)
Planck Collaboration et al., 2015a, preprint, (arXiv:1502.01591)
Sánchez C., et al., 2014, MNRAS, 445, 1482
Schrabback T., et al., 2007, A&A, 468, 823
Sheldon E. S., 2014, MNRAS, 444, L25
Smith R. E., et al., 2003, MNRAS, 341, 1311
Smith K. M., Zahn O., Doré O., 2007, Phys. Rev. D, 76, 043510
Story K. T., et al., 2013, ApJ, 779, 86
Takahashi R., Sato M., Nishimichi T., Taruya A., Oguri M., 2012, ApJ, 761, 152
The Dark Energy Survey Collaboration et al., 2015, preprint, (arXiv:1507.05552)
Troxel M. A., Ishak M., 2015, Phys. Rep., 558, 1
Vallinotto A., 2013, ApJ, 778, 108
Van Waerbeke L., et al., 2000, A&A, 358, 30
Wittman D. M., Tyson J. A., Kirkman D., Dell'Antonio I., Bernstein G., 2000, Nature, 405, 143
Zuntz J., Kacprzak T., Voigt L., Hirsch M., Rowe B., Bridle S., 2013, MNRAS, 434, 1604
Zuntz J., et al., 2015, Astronomy and Computing, 12, 45
van Daalen M. P., Schaye J., Booth C. M., Dalla Vecchia C., 2011, MNRAS, 415, 3649
van Engelen A., et al., 2012, ApJ, 756, 142

AFFILIATIONS

[1] *Department of Physics and Astronomy, University of Pennsylvania, Philadelphia, PA 19104, USA*
[2] *Institute of Astronomy, University of Cambridge, Madingley Road, Cambridge CB3 0HA, UK*
[3] *Kavli Institute for Cosmology, University of Cambridge, Madingley Road, Cambridge CB3 0HA, UK*
[4] *Centre for Theoretical Cosmology, DAMTP, University of Cambridge, Wilberforce Road, Cambridge CB3 0WA, UK*
[5] *Fermi National Accelerator Laboratory, P. O. Box 500, Batavia, IL 60510, USA*
[6] *Kavli Institute for Cosmological Physics, University of Chicago, Chicago, IL 60637, USA*
[7] *Department of Physics, University of Michigan, Ann Arbor, MI 48109, USA*
[8] *Department of Physics, University of Chicago, 5640 South Ellis Avenue, Chicago, IL 60637, USA*
[9] *Argonne National Laboratory, Argonne, IL, 60439, USA*
[10] *Department of Astronomy and Astrophysics, University of Chicago, Chicago, IL 60637, USA*
[11] *Institut de Ciències de l'Espai, IEEC-CSIC, Campus UAB, Carrer de Can Magrans, s/n, 08193 Bellaterra, Barcelona, Spain*
[12] *Department of Physics & Astronomy, University College London, Gower Street, London, WC1E 6BT, UK*
[13] *Institut de Física d'Altes Energies (IFAE), The Barcelona Institute of Science and Technology, Campus UAB, 08193 Bellaterra (Barcelona) Spain*
[14] *Department of Physics, Stanford University, 382 Via Pueblo Mall, Stanford, CA 94305, USA*
[15] *Kavli Institute for Particle Astrophysics & Cosmology, P. O. Box 2450, Stanford University, Stanford, CA 94305, USA*
[16] *Jodrell Bank Center for Astrophysics, School of Physics and Astronomy, University of Manchester, Oxford Road, Manchester, M13 9PL, UK*
[17] *Cerro Tololo Inter-American Observatory, National Optical Astronomy Observatory, Casilla 603, La Serena, Chile*
[18] *Department of Physics and Electronics, Rhodes University, PO Box 94, Grahamstown, 6140, South Africa*
[19] *Department of Astrophysical Sciences, Princeton University, Peyton Hall, Princeton, NJ 08544, USA*
[20] *CNRS, UMR 7095, Institut d'Astrophysique de Paris, F-75014, Paris, France*
[21] *Sorbonne Universités, UPMC Univ Paris 06, UMR 7095, Institut d'Astrophysique de Paris, F-75014, Paris, France*
[22] *Carnegie Observatories, 813 Santa Barbara St., Pasadena, CA 91101, USA*
[23] *Laboratório Interinstitucional de e-Astronomia - LIneA,*

Rua Gal. José Cristino 77, Rio de Janeiro, RJ - 20921-400, Brazil
[24] *Observatório Nacional, Rua Gal. José Cristino 77, Rio de Janeiro, RJ - 20921-400, Brazil*
[25] *Department of Astronomy, University of Illinois, 1002 W. Green Street, Urbana, IL 61801, USA*
[26] *National Center for Supercomputing Applications, 1205 West Clark St., Urbana, IL 61801, USA*
[27] *Department of Physics, McGill University, 3600 rue University, Montreal, QC, H3A 2T8, Canada*
[28] *Excellence Cluster Universe, Boltzmannstr. 2, 85748 Garching, Germany*
[29] *Faculty of Physics, Ludwig-Maximilians-Universität, Scheinerstr. 1, 81679 Munich, Germany*
[30] *Department of Astronomy, University of Michigan, Ann Arbor, MI 48109, USA*
[31] *SLAC National Accelerator Laboratory, Menlo Park, CA 94025, USA*
[32] *Department of Physics, University of California, Berkeley, CA, 94720, USA*
[33] *Center for Cosmology and Astro-Particle Physics, The Ohio State University, Columbus, OH 43210, USA*
[34] *Department of Physics, The Ohio State University, Columbus, OH 43210, USA*
[35] *Australian Astronomical Observatory, North Ryde, NSW 2113, Australia*
[36] *Departamento de Física Matemática, Instituto de Física, Universidade de São Paulo, CP 66318, CEP 05314-970, São Paulo, SP, Brazil*
[37] *George P. and Cynthia Woods Mitchell Institute for Fundamental Physics and Astronomy, and Department of Physics and Astronomy, Texas A&M University, College Station, TX 77843, USA*
[38] *Department of Astronomy, The Ohio State University, Columbus, OH 43210, USA*
[39] *Institució Catalana de Recerca i Estudis Avançats, E-08010 Barcelona, Spain*
[40] *Max Planck Institute for Extraterrestrial Physics, Giessenbachstrasse, 85748 Garching, Germany*
[41] *Jet Propulsion Laboratory, California Institute of Technology, 4800 Oak Grove Dr., Pasadena, CA 91109, USA*
[42] *School of Physics, University of Melbourne, Parkville, VIC 3010, Australia*
[43] *Department of Physics and Astronomy, Pevensey Building, University of Sussex, Brighton, BN1 9QH, UK*
[44] *Centro de Investigaciones Energéticas, Medioambientales y Tecnológicas (CIEMAT), Madrid, Spain*
[45] *Brookhaven National Laboratory, Bldg 510, Upton, NY 11973, USA*
[46] *Harvard Smithsonian Center for Astrophysics, 60 Garden St, MS 12, Cambridge, MA, 02138, USA*
[47] *Institute of Cosmology & Gravitation, University of Portsmouth, Portsmouth, PO1 3FX, UK*

This paper has been typeset from a TEX/LATEX file prepared by the author.